Journal of
Nanotheranostics

MDPI

Review

Use of Superparamagnetic Iron Oxide Nanoparticles (SPIONs) via Multiple Imaging Modalities and Modifications to Reduce Cytotoxicity: An Educational Review

Nicholas R. Nelson, John D. Port and Mukesh K. Pandey *

Department of Radiology, Mayo Clinic, Rochester, MN 55905, USA; sa200331@atsu.edu (N.R.N.); Port.John@mayo.edu (J.D.P.)

* Correspondence: Pandey.Mukesh@mayo.edu; Tel.: +1-507-538-4221; Fax: +1-507-266-4461

Received: 5 November 2020; Accepted: 4 December 2020; Published: 9 December 2020

Abstract: The aim of the present educational review on superparamagnetic iron oxide nanoparticles (SPIONs) is to inform and guide young scientists and students about the potential use and challenges associated with SPIONs. The present review discusses the basic concepts of magnetic resonance imaging (MRI), basic construct of SPIONs, cytotoxic challenges associated with SPIONs, shape and sizes of SPIONs, site-specific accumulation of SPIONs, various methodologies applied to reduce cytotoxicity including coatings with various materials, and application of SPIONs in targeted delivery of chemotherapeutics (Doxorubicin), biotherapeutics (DNA, siRNA), and positron emission tomography (PET) imaging applications.

Keywords: superparamagnetic iron oxide nanoparticles (SPIONs); iron oxide nanoparticles (IONPs)

1. Overview of Magnetic Resonance Imaging

Magnetic resonance imaging (MRI) is a common biomedical technique used to provide images of the soft tissues within the body that contain water [1]. This is accomplished by first placing a patient or biomedical sample into an external magnetic field that is commonly 0.5–3 Tesla in the clinical practice and up to 10.5 Tesla for research studies [1], causing the magnetic poles of the water protons to align with the field. Next, a short radiofrequency (RF) pulse is applied with a frequency matching the resonant frequency of the hydrogen nucleus. Once the RF pulse is completed, the protons in the patient/sample emit an RF signal that is detected by the MRI machine [2] (Figure 1); this is the signal that is used to create the MR images. A brief delay between RF pulses allows the protons to realign (relax) parallel with the external magnetic field before disturbing the orientation again with the next RF pulse [2]. This process is repeated many times, applying the many different spatial encodings necessary to reconstruct an image from the emitted RF signals.

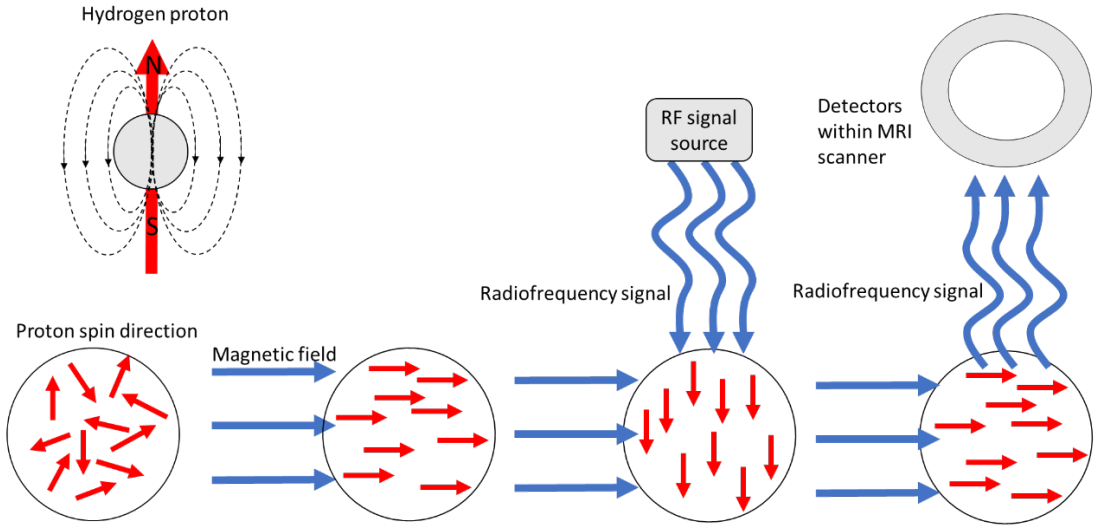

Figure 1. Pictorial representation of MRI signal acquisition.

The relaxation time of the tissue is defined as the time it takes for the protons to return to their initial (baseline) configuration in the strong external magnetic field after being maximally stimulated by the RF pulse. For human tissue and samples, two major types of relaxation are commonly used. The time it takes for the magnetic poles on the protons in a tissue to realign with the main magnetic field is called longitudinal (spin-lattice) relaxation and is designated as the T1 relaxation time. The time it takes for the magnetic poles on the protons in a tissue to de-phase (e.g., spin out of phase with each other) is called transverse (spin-spin) relaxation, and is designated as the T2 relaxation time. Each tissue in the body has characteristic T1 and T2 relaxation times dependent upon the tissue type and density; physicians use these relaxation differences to distinguish among different tissues and to diagnose diseases [2]. In a similar fashion, biological compounds also have characteristic T1 and T2 relaxation times depending on the chemical structure of the compound and surrounding solvent. Finally, the relaxation rate of a tissue or compound is defined as (R1 = 1/T1 and R2 = 1/T2), meaning that a compound with a high r1 and r2 will have a low T1 and T2 [2].

To enhance the imaging capabilities of MRI, contrast agents such as gadolinium (Gd(II)) and more commonly (Gd(III)) complexes have been used to increase the speed of proton realignment with the magnetic field [2], acting to shorten the T1 time (increase the r1 value) of the water molecules surrounding the Gd complexes. This shorter T1 time leads to a brighter signal on the MRI images acquired to detect changes in T1 (so-called T1-weighted imaging); as such, gadolinium and related compounds are said to exhibit positive contrast on T1-weighted images. Unfortunately, free gadolinium is highly toxic to humans; accumulation of gadolinium in the tissues can cause nephrogenic systemic fibrosis (NSF) in patients with poor renal function [2]. NSF has been shown to be caused by the transmetallation or dechelation of Gd complexes in vivo [3]. Free Gd ion uptake in macrophages and fibrocytes may lead fibroblast growth and lead to the changes seen in skin, joints, and internal organs during NSF [4]. Macrocyclic Gd-based contrast agents are more stable than the linear agents due to greater kinetic stability, leading to less detectable gadolinium deposition [5,6]. Gd-chelation agents have received attention as gadolinium deposition has been seen in a concentration-dependent relationship in the dentate nucleus and globus pallidus regions of the brain, independent of patients' renal function [7–10]. Beyond the brain, Gd-based contrast agents have also been observed in the bone five years post-injection [11], or in the liver, skin, spleen, and kidney [12]. Despite all the studies showing the accumulation of Gd in various tissues, the role of Gadolinium Deposition Disease causing clinical manifestations has not been clearly demonstrated [13]. Instead of injecting free ions, gadolinium is typically encapsulated within proteins, liposomes, and dendrimers where it is sequestered away from the tissues. Additional drawbacks of using Gd complexes also include the confinement of Gd

complexes to the blood and extracellular space with unfavorable cellular uptake and a short blood circulation half-life [2]. Manganese(II) complexes have also been tested for use as a contrast agent for MRI imaging, but they are shown to exhibit high cardio and pulmonary toxicity with inferior thermodynamic stability, magnetization, and MRI signal sensitivity compared to Gd complexes [2,14].

2. Use of Superparamagnetic Iron Oxide Nanoparticles (SPIONs) in Magnetic Resonance Imaging (MRI)

Superparamagnetic iron oxide nanoparticles (SPIONs), like Endorem and Resovist used for imaging liver lesions via MRI, are composed of small superparamagnetic Fe_3O_4 iron oxide cores and coated with biocompatible layers such as dextran or carbodextran [15,16]. Superparamagnetic behavior is the ability of the nanoparticles to flip the orientation of the protons within their core rapidly when exposed to and disengaged from an external magnetic field, giving SPIONs very high relaxivity values [2]. This behavior arises due to the coupling of proton spin with unpaired 3d electrons in the Fe^{3+} and Fe^{2+} cations within the cubic fcc lattice [2] (Figure 2). Once located within the proper tissue, the SPIONs introduce a local field inhomogeneity to cause negative contrast on T2-weighted imaging by shortening T2 relaxation (unlike paramagnetic agents such as gadolinium which create positive contrast by shortening T1 relaxation [17]).

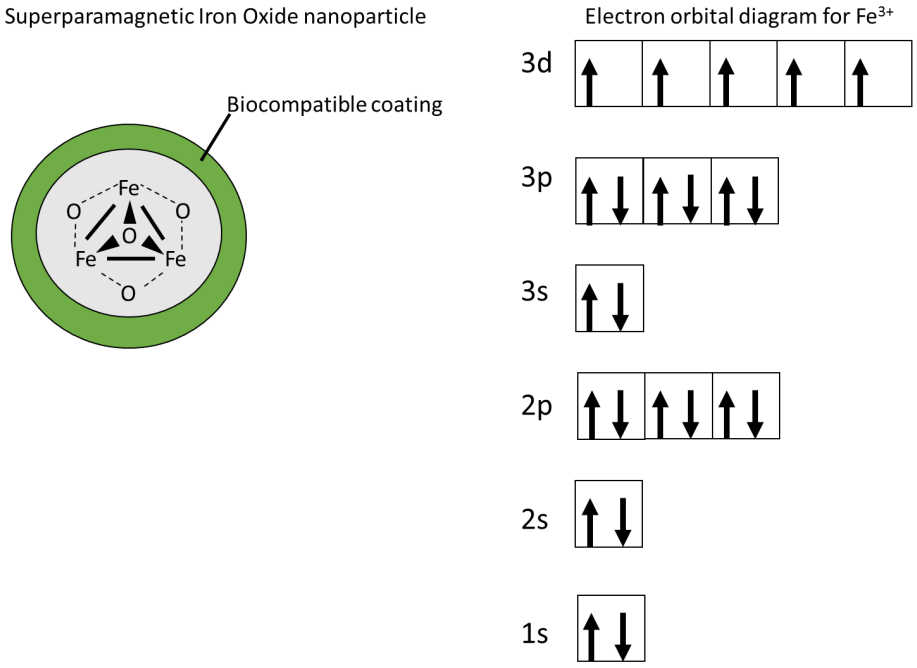

Figure 2. Pictorial representation of Fe_3O_4 lattice structure and orbital electron spin of Fe^{3+} in iron oxide.

In the laboratory, to determine if a particle exhibits paramagnetic behavior, a hysteresis loop is conducted where the particle is subjected to a magnetic field with increasing strength until the particle reaches the saturation magnetization value where the particle cannot be magnetized any further [18]. The strength of the magnetic field is then gradually removed until it becomes zero and then increased in the opposite direction until the particle reaches the saturation magnetization value in the opposite direction before removing the magnetic field again [18]. The magnetization of the particle vs. the strength of the external magnetic field at various time points is plotted and examined to observe if the particle exhibits a hysteresis curve [18] (Figure 3). A hysteresis curve shows that the particle is ferromagnetic rather than paramagnetic and is when the particle exhibits magnetization at a time point when the applied external field is zero [18]. Superparamagnetic particles show saturation magnetization values that are much higher than the values for paramagnetic particles at equal magnetic field strength [18].

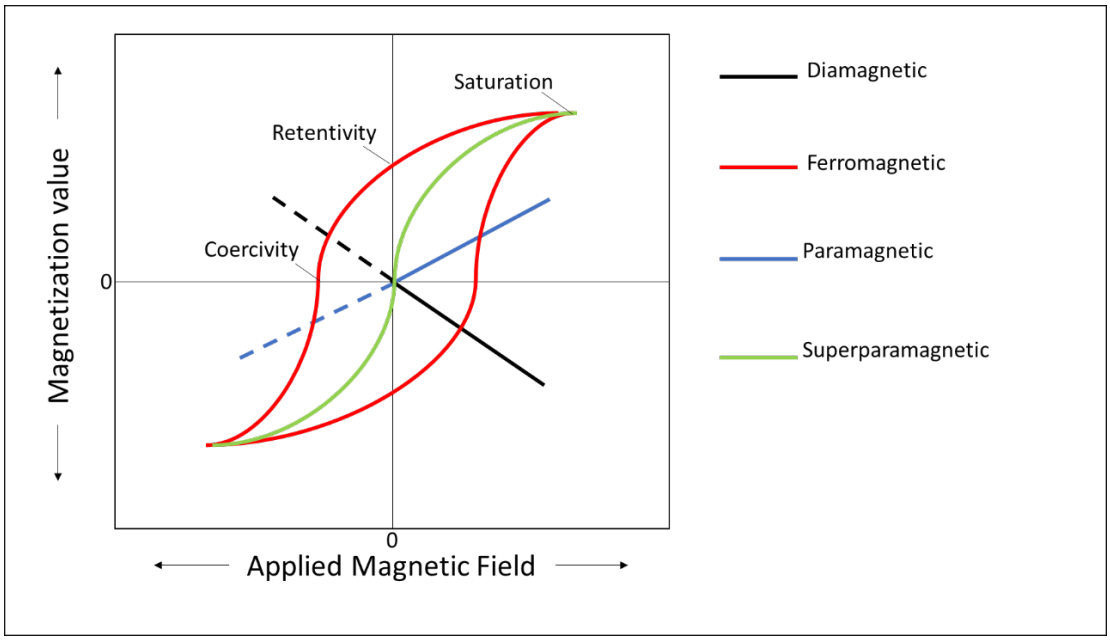

Figure 3. Hysteresis curve representing the relationship between magnetization value and applied magnetic field for the diamagnetic, ferromagnetic, paramagnetic, and superparamagnetic particles.

The size of the SPION and the biocompatible coating is crucial in determining the superparamagnetic capabilities of the particle. Ideally, the SPIONs would have a narrow size distribution along with uniform physical and chemical properties to provide a consistent and homogenous signal via MRI [18]. For polyethylene glycol (PEG) coated SPIONs 40–50 nm in diameter the saturation magnetization was found to be between 45 and 50 electromagnetic units per gram (emu/g) [18], while for uncoated 16 nm particles the saturation magnetization was 67.8 emu/g [19]. The clinically available SPION Feridex IV has a hydrodynamic diameter (HD) larger than 50 nm and distributes to the reticuloendothelial system (RES), while ultrasmall SPIONs like ferumoxtran-10 with an HD less than 50 nm can distribute to both the RES and the lymph nodes [8]. The benefit of having a larger diameter results in an increase in the negative contrast provided in T2-weighted images [20,21], but may change the even biodistribution throughout the body. For SPIONs between 10 and 15 nm, there are 62,896 atoms within each SPION and 1.71×10^{17} SPIONs within 1 g [18].

In addition to the unique superparamagnetic behavior of SPIONs, their small size also allows them to display useful distribution behavior throughout the body. Along with possessing a superior T1 contrast and having a nontoxic nature [22], SPIONs also provide details on the mechanisms of disease progression and therapeutic efficiency of drugs better than the traditional Gd based contrast agents Gd-DPTA and Gd-DOTA due to the ability of SPIONs to become phagocytosed instead of remaining in the extracellular space [23]. By becoming phagocytosed by macrophages, SPIONs can measure Rheumatoid arthritis severity due to its correlation with the abundance/activation of macrophages [23]. However, it has been shown that the location of the SPION injection may have a significant impact on SPION distribution as well. Intravenous (I.V.) injected SPIONs with a polyvinyl alcohol (PVA) coating showed specific uptake in the arthritic joint without uptake in the control contralateral joint for seven days, while intra-articular (I.A.) injection did not show specific uptake and remained in the synovial lining of both joints for 14 days [24]. In addition to phagocytosis, SPIONs may also undergo a process that occurs more rapidly called nanoparticle-induced endothelial leakiness where the SPION induces gaps of over 10 μm in size between endothelial cells by rearranging the cytoskeleton via the binding and phosphorylation of VE-cadherin [25] (Figure 4a).

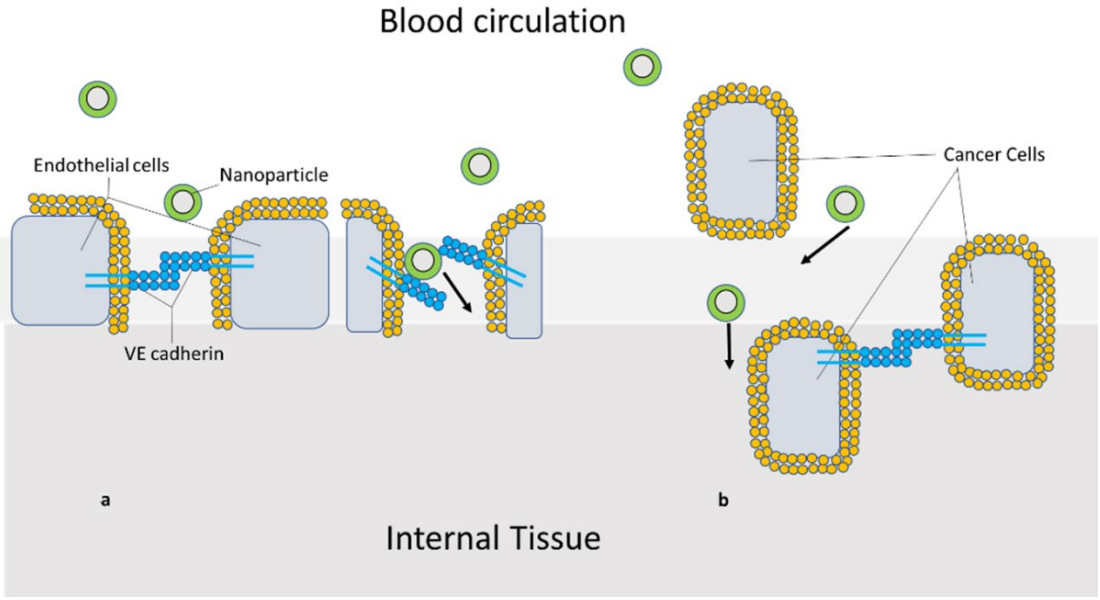

Figure 4. Pictorial representation of nanoparticle-induced endothelial leakiness (**a**) compared to extravasation through perforated vasculature in tumor (cancer) tissue (**b**).

SPIONs have also been shown to be useful in targeting cancerous tissue through a condition called the enhanced permeation retention (EPR) effect. The EPR effect arises due to the perforated vasculature and weak lymphatic drainage of tumor tissue, which allows intravenously injected nanoparticles to extravasate and preferentially accumulate in the tumor tissue [26] (Figure 4b). However, the EPR effect may not always be relied upon to passively target tumors, because the vasculature permeability varies between different tumors and even within areas of the same tumor [26] resulting in the usual distribution of 95% or more of the injected dose per tumor in normal tissues [27]. Due to this, iron oxide nanoparticles (IONPs) in clinical use typically remain in the blood from 1 to 24–36 h before being cleared by the RES [28].

3. Toxicity and Modification of SPIONs

3.1. Oxidative Damage

A large concern with the use and safety of SPIONs involves the possible cytotoxic effects of the particles caused by IONP-induced oxidative stress. After phagocytosis and the further fusion of the phagosome with a lysosome, IONPs are degraded due to the acidic environment and may release free Fe^{2+} into the cell's lysosome or cytoplasm [29]. This free Fe^{2+} can then lead to the induction of DNA damage or inflammatory responses through the generation of reactive oxygen species (ROS) via the Fenton reaction [30]. Under normal conditions, the frequency of ROS generation via coupling conditions in the mitochondrion is low enough to be easily neutralized by glutathione (GSH) and antioxidant enzymes [31].

When the ratio of GSH to oxidized glutathione is low, oxidative stress occurs and the cells respond by creating protective or injurious responses [31–34]. When cells are at a low level of oxidative stress, the transcription factor Nrf-2 causes the induction of antioxidant and detoxification enzymes but at higher levels of oxidative stress, the cell response is less protective and more cytotoxic leading to inflammation through the mitogen-activated protein kinase (MAPK) and nuclear factor kB (NF-kB) cascades [34]. To help combat the excess of catalytically active iron, the cells rely on a variety of proteins to regulate the internal concentration of iron (Figure 5). Divalent Metal Transporter 1 (DMT1) assists the import of free iron into the cell, while transferrin is imported into the cell through CD71 and Ferritin (FTH) sequester iron within the cell and reduce the ability of the iron to form free radicals [35].

To eliminate iron, Ferroportin (FPN) and ZRT-IRE like proteins are used to export iron from the cell [35]. While these proteins function well under normal conditions to control the internal concentration of iron, the ability of IONPs to diffuse directly into the labile iron pool via the phagosome to lysosome route gives the potential for IONPs to overload these regulatory proteins [36]. Since high ROS production has the potential to lead to cell injury and death [37] along with the oxidation of proteins, DNA, and lipids [38] researchers evaluating the safety of emerging IONPs should closely monitor the biomarkers of oxidative stress including lipid peroxidation, reduced glutathione, superoxide dismutase, and the antioxidant enzymes including catalase, glutathione S transferase, glutathione peroxidase, and glutathione reductase to determine the cytotoxicity of various IONPs [39]. Confirming that this cytotoxicity is due to free iron released from IONPs and not another component of the nanoparticle, the effects of increased LDH, ROS, and DNA damage were all avoided after using an iron chelator [40]. While studies have shown that uncoated IONPs show significant oxidative stress in rats [39], it is important to note that the type of macrophages chosen has a significant effect as well with mouse alveolar macrophages showing low activity vs. the peritoneal macrophages [41].

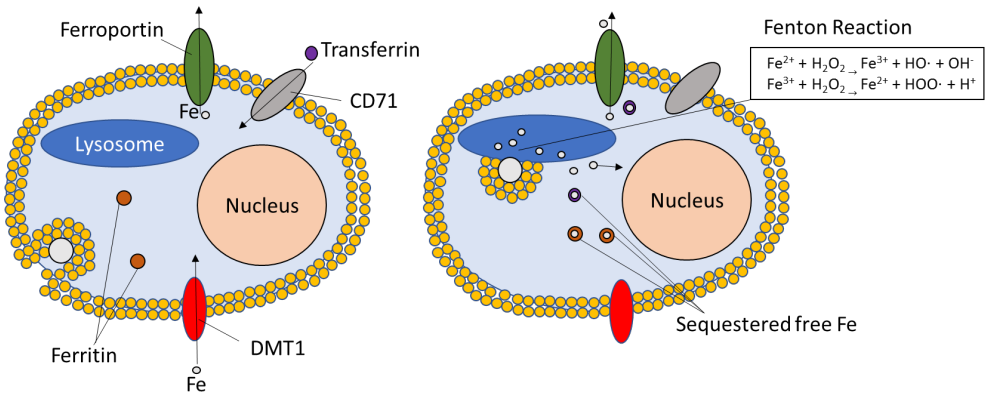

Figure 5. Pictorial diagram showing the release of free Fe^{2+} ions from IONPs and intracellular sequestration of free Fe^{2+} ions via Ferritin and Transferrin.

3.2. Unique Size/Shape Toxicity

The small size exhibited by SPIONs leads to a large surface area to mass ratio and more groups on the particle surface that may react and induce cytotoxic effects [42]. This cytotoxicity vs. particle size effect is even pronounced among different SPIONs, where smaller SPIONs show increased cytotoxicity on a per mass basis [43,44]. Contrary to this behavior, rod-shaped nanoparticles with less surface area have been shown to be more toxic than spherical nanoparticles, suggesting that the amount of surface area is not always the most important factor in determining the degree of cytotoxicity [45]. Other factors that have also been shown to affect the cytotoxicity of SPIONs include the pH of the dosing media [46] particle composition, shape, surface coatings, and overall charge of the SPIONs [47]. Together these cytotoxic effects may combine to induce a 15% decrease in cell viability in human fibroblasts along with increased ROS generation for 50 nm Fe_2O_3 concentrations of only 2 μg/cm^2, while the 10 and 50 μg/cm^2 concentrations induced DNA damage [48]. Although clustered nanoparticles provide enhanced r2 values [49], care should also be taken to prevent large aggregations of IONPs. When Fe_2O_3 is allowed to aggregate in large sizes up to 934 to 1444 nm, double-stranded DNA breaks can be seen at IONP concentrations as low as 3.03 μg/cm^2 [50]. The cytotoxicity of IONPs becomes even more severe when using the highly soluble Fe_3O_4 composition instead of the commonly used and less soluble Fe_2O_3 [41]. Studies evaluating the cytotoxicity of IONPs have also found no cytotoxicity or DNA damage for α-Fe_2O_3 in sizes 87, 238, or 1100 nm and concentrations of 20–100 μg/cm^2 [51]. This seems to largely contradict the studies included above; however, IONPs have been shown to possess the ability to interfere with cytotoxicity assays [52] cytokine secretion assays [53], as well as other possible assays.

The size of SPIONs along with the surface chemistry and charge can also be altered to affect the clearance from the body as well as cytotoxicity due to the altering of phagocytosis of SPIONs by cells and binding of SPIONs to proteins. By modifying the size and charge of SPIONs before injection, the adsorption and opsonization by serum proteins can also be altered [47]. After a SPION is adsorbed or opsonized by a serum protein, its hydrodynamic diameter increases to cause a lower rate of glomerular filtration and a longer blood and whole body half-life [47] due to the small effective pore sizes of 5 nm in the vascular endothelial layer and 6 nm in the lymphatic vessel endothelial layer in the glomerulus [54,55]. In addition to serum proteins, nanoparticles can also bind to other proteins to form a complex with increased tissue penetration and altered function from the catalytically driven splitting of intramolecular or intermolecular bonds on the nanoparticle surface [42]. Together, these changes lead to the potential for injurious responses by allowing SPIONs to travel throughout the body with increased endocytosis while penetrating organs and tissues that they would not normally be able to without a SPION-protein complex being formed [42].

3.3. Site-Specific Accumulation

The excretion of SPIONs primarily occurs through either the renal pathway or the hepatobiliary system. Since the hepatobiliary system has a greater potential for cytotoxicity due to the intracellular enzymatic modification pathway of excretion, the renal pathway is commonly preferred to avoid cytotoxicity [47]. To optimize SPIONs for excretion through the renal pathway they must be able to pass through the fenestrate, glomerular basement, and filtration slits with a combined physiologic pore size of only 4.5 to 5 nm in diameter [56,57]. While this allows for the easy excretion of particles less than 4.5 nm through the renal pathway, cationic particles with HD from 6–8 nm may still pass through the pores [56]. Care must be taken however to ensure that SPIONs are not entirely cationic or anionic, which will cause the HD to be increased by charge-related adsorption by serum proteins [54]. This shifts the pathway of excretion from the kidneys to the liver, which is commonly used to clear virus sized particles between 10 to 20 nm from the blood stream [54].

Another aspect to take into consideration for the toxicity of SPIONs is that they do not distribute evenly throughout the body by preferentially accumulating in specific organs or tissues (Figure 6). To promote longer blood circulation times for best imaging results, SPIONs should be less than 200 nm to avoid mechanical filtration and sequestration in the spleen while still remaining larger than 10 nm to avoid rapid clearance through the kidneys [58]. While this size works well for blood circulation times, this small size of SPION can also become problematic for achieving an even distribution throughout the body and avoiding cytotoxicity. Due to the small size and large hydrophobic surface area, SPIONs tend to agglomerate before being taken up by macrophages in the liver called Kupffer cells as well as other plasma proteins of the body's reticuloendothelial system (RES) [18]. Once activated, macrophages produce and secrete inflammatory molecules to recruit cells from the innate and adaptive immune system along with cells that are designed to kill ingested microbes through the generation of ROS called an "oxidative burst" [59]. A remarkable property of macrophages is that after macrophages engulf foreign particles such as SPIONs they may distribute throughout the body and enter any tissue before specializing to become Kupffer cells in the liver, osteoclasts in the bone, microglial cells in the brain, alveolar macrophages in the lungs, or mesangial cells in the kidney [59]. A common approach to enhance the EPR effect and avoid the SPION cytotoxicity caused by uptake via cells of the RES is to cover SPIONs with amphiphilic polymeric surfactants like poly(ethylene glycol) (PEG) that also selectively provide increased interaction with the cell membranes of cells in the target tissue[18], which will be discussed in further detail.

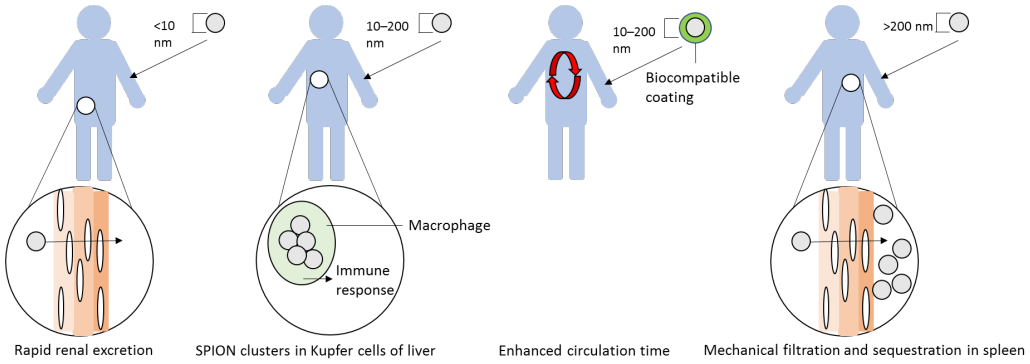

Figure 6. Pictorial diagram showing size-based excretion and effects of SPION on the human body.

3.4. Pulmonary Exposure Results

While many studies have focused on the intratracheal installation of iron oxide and pulmonary exposure, extrapulmonary cytotoxicity can also be observed in these studies due to the small size of IONPs that allows them to enter the bloodstream in less than 10 min before settling in the liver, spleen, and kidney [60]. Human studies measuring the cytotoxicity following pulmonary exposure to iron oxide dust however are difficult to draw conclusions from due to the presence of other particles in the air such as quartz or silica and the unregulated size of the iron oxide particles [36].

3.4.1. Mechanisms

To activate lung immune cells and remove the foreign material, an inflammatory response occurs immediately after a foreign particle is introduced into the lungs via inhalation [36]. This response is seen by the elevated levels of proinflammatory cytokines IL-6 and IL-8 [61] and the ability of macrophages to switch from the anti-inflammatory subtype M1 to the pro-inflammatory macrophage subtype M2 after incubation with nanoparticles [62,63]. While under normal circumstances this response would effectively minimize tissue injury and damage [36], IONPs have the ability to induce chronic inflammation [64] that can lead to cancer, fibrosis [36,65], or a pulmonary allergic reaction [66,67] if the particle is not cleared from the lungs. The induction of pulmonary fibrosis is a well-studied result of cytokines being released during the inflammatory response with TGF-β leading to the increase in collagen production via alveolar fibroblasts [68]. If this process becomes excessive or dysregulated, the increased collagen tissue in the lungs causes irreversible scarring and reduces the elasticity and volume of pulmonary air intake [36].

3.4.2. Animal Studies

Animal studies performed to assess the cytotoxicity of iron oxide particles have largely used rats and mice. When ICR mice are given a single intratracheal instillation of 5.3 nm Fe_3O_4 up to 0.02 mg/mouse there is an acute inflammatory response one-day post exposure, and lower but still significantly elevated inflammatory cytokine levels up to 28 days post exposure [69]. In addition to this, other measurements of this study also found increased expression of genes related to inflammation and tissue damage along with a reduction in glutathione and the formulation of micro granulomas [69]. Contrary to these cytotoxicity findings, one study showed that when the diameter was kept below 50 nm for Wistar rats intratracheally instilled at 1 or 5 mg/kg body weight, only weak signs of pulmonary fibrosis and no cytotoxicity outside of the lungs was observed 30 days after exposure [70]. It has also been demonstrated that a single 2 mg/kg intratracheal instillation of 209 nm agglomerated particles may remain in the lungs even longer after exposure by observing them engulfed within alveolar macrophages at 90 days post exposure to ultimately initiate a Th1 polarized immune response [64]. Pulmonary inflammation along with hepatic enzymes in the blood indicating liver damage was also seen for smaller sized Fe_2O_3 particles given with a higher number of doses where 20 mg/kg of 20 nm

Fe_2O_3 was intratracheally instilled seven times every other day [71]. Instead of dosing via intratracheal instillation, Windstar rats were also dosed for 4 h via head and nose inhalation of Fe_3O_4 particles that were 15 to 20 nm in size at a concentration of 640 mg/m^3 of air [72]. This showed increased levels of the biomarkers related to cytotoxicity and inflammatory responses such as LDH, neutrophil infiltration, and pro-inflammatory cytokines. IONP induced oxidative stress was also indicated by a reduction in GSH and antioxidant enzyme activities [72]. Interestingly, IONPs can also cause a decrease in inflammation-most likely due to ROS-induced cell death [67]. A lower number of neutrophils, eosinophils, and lymphocytes were observed when Fe_2O_3 was intratracheally instilled at 2.5 mg/kg into Balb/c mice that were previously sensitized with ovalbumin (OVA) [67]. This IONP regulated effect on inflammation was shown to be controlled by the concentration of IONP when the allergic response induced by OVA was inhibited by middle and high doses of IONPs but was enhanced at the lowest dose used for treatment [66].

3.4.3. Genotoxicity

While pulmonary fibrosis and oxidative stress are serious potential consequences of IONP exposure, a few studies involving exposure to IONPs have shown even more severe cytotoxicity such as genotoxicity leading to the formation or promotion of cancer. The covalent coupling of DNA linked to a carcinogenic compound is known as DNA adducts, which was seen only 24 h after intratracheal instillation of 10 nm Fe_3O_4 in concentrations of 0.05 mg per ICR mice [73]. At the same concentration and particle size, gpt delta mice showed DNA damage through increased gpt mutations as well as lipid peroxidation-related DNA adducts, inflammatory cell infiltration, and the formation of focal granulomas [73]. When examining the effects of long term chronic exposure to iron oxide, the induction of primary lung tumors 800 days post exposure was seen for groups of 8 to 10 mice compared to controls [74]. These mice were exposed to 0.5 g $Fe_2O_3 \cdot H_2O$ that was uncharacterized in size for 6 h a day, five days a week, over an entire year to simulate an occupational exposure to iron oxide particles [74]. Another long-term exposure study demonstrated that cells treated with IONPs at 0.6 μg/cm^2 continuously for 10 weeks showed significant features of cancer cells including an increase in cell proliferation, formation of anchorage-independent colonies, and immortalization [50]. In addition to DNA lesions, an increase in expression of genes related to cation/metal binding, membrane formation, and morphogenesis was also seen in zebrafish when exposed to 4.6 mg/L IONP that were coated in meso-2, 3-dimercaptosuccinic acid (DMSA) [75]. When the concentration of IONPs becomes as high as 200 mg/kg, a decrease in acetylcholinesterase activity and the induction of apoptosis is seen within the brain of zebrafish [76].

3.5. Human Studies

Human studies to assess the in vivo cytotoxicity have largely revolved around occupational exposure to iron oxide particles found in the air. Underground iron ore miners with poor ventilation are at high risk for this exposure and were found to have around a 75% increased risk of lung cancer related death [77]. The limits of this study, however, were the presence of radon daughters and the uncharacterized IONP size within the circulating air. Another occupational group that is at high risk for iron oxide particle exposure is welders who showed increased fibrotic lesions and elevated lung iron levels as well as iron oxide, manganese oxide, and chromium oxide particulates internalized within alveolar macrophages [78].

4. Coatings

Care should be taken when evaluating new SPION formulations as they can interact with the enzymatic cascades in the blood including coagulation pathways, complement system, and kallikrein-kinin system (KKS). When a foreign material enters a host, a process called opsonization occurs rapidly where the foreign material accumulates a layer of host proteins before the arrival of inflammatory cells. Adsorbed fibrinogen, crucial to the accumulation of phagocytes, can be recognized

by phagocytes as a fibrin clot and lead the phagocytes to trigger responses designed to initiate wound healing at a site of vascular injury [79]. Adsorbed fibrinogen causes platelet adherence and may be displaced by high-molecular-weight-kininogen and FXII of the clotting cascade [80]. The unfolding of adsorbed fibrinogen during opsonization can also lead to changes in antibody binding or epitope exposure, further driving coagulation and inflammation [81]. Inflammatory responses introduced by SPIONs can alter the hemocoagulation equilibrium by either favoring thrombosis or bleeding. When an inflammatory response occurs, tissue factor (TF) is expressed intravascularly on monocytes and endothelial cells are activated by proinflammatory cytokines. Activated TF may then complex with activated FVII to activate FX and FIX [82]. The kallikrein-kinin system assists in activating the intrinsic coagulation pathway and alters the activated partial thromboplastin time (APTT) [82]. Negatively charged materials including glass, kaolin, and celite can stimulate the KKS leading to FXII autoactivation. Activated FXII then forms a positive feedback loop and activates prekallikrein to kallikrein. This may manifest clinically as hypotension, angioedema, hyperfibrinolysis, and the stimulation of the complex inflammatory response [82]. Dextran-coated SPIONs should be evaluated with caution as the binding of plasma prekallikrein and high-molecular weight-kininogen (HK) to uncoated sites of the iron oxide core of dextran-coated SPIONs may occur, leading to the activation of the kallikrein-kinin system [83,84]. Polyvinyl alcohol (PVA) coated SPIONs were previously shown to raise the levels of the inflammatory cytokine IL1β, but this effect was minimized after eliminating free-floating PVA and reducing the zeta potential of the coated SPIONs [85].

When comparing polyacrylic acid (PAA), hyaluronic acid (HA), and chitosan (CS) as coatings for SPIONs there was increased interaction demonstrated between blood and PAA-coated SPIONs [86]. This presented with RBC hemolysis rates of 23% compared to 7.5% for HA and 5.1% for CS. The PAA-coated SPIONs also demonstrated the highest degree of RBC membrane damage, aggregated platelets, and significantly lengthened prothrombin time, activated partial thromboplastin time, and thrombin time compared to HA and CS coatings [86]. While the prolonged coagulation time was due to the loss of one or several coagulation factors, the increase in activated C3 of the classical pathway of the complement system was theorized to be due to the abundant -OH and -COOH groups of PAA [86].

In a separate study, PEG coating of IONPs showed increased adsorption and activation of the complement system with an increased concentration of the C3a, C4a, C5a, C5b-9, IL-1B, IL-6, and TNF-α compared to polyvinylpyrrolidone and uncoated IONPs. The soluble byproducts of complement activation C3a, C4a, and C5a are known as anaphylatoxins. They work by inducing inflammation either locally or in other tissues. C5b-9 binds and polymerizes many copies of C9 to form a pore in the cell membrane allowing free diffusion of molecules in and out of the cell, leading to cell death [87]. Together, these studies emphasize the importance of the coating when evaluating the safety and biocompatibility of SPIONs. Although IONPs of small size show very little to no cytotoxicity at concentrations below 100 mg/mL [88], this behavior has the potential to change for aggregates due to the increased size of the particles. Since uncoated SPIONs have a large tendency to aggregate or precipitate in saline at concentrations of 3 mg/mL for SPIONs 16 nm in size [19], a large amount of research has gone into developing coatings for SPIONs to prevent this aggregation and precipitation while avoiding cytotoxicity. These coatings may be composed of a variety of materials including PEG [18], chitosan [89], dextran [90], as well as other polymers [91]. The high molecular weight coatings PEG, PVA, and dextran work to prevent aggregation of SPIONs by interfering with the strong magnetic dipole-dipole interactions between the iron oxide cores [92] (Figure 7a). An additional advantage of encapsulating SPIONs in coatings is the ability to increase relaxation times for better imaging results [93] and prevent or delay the release of Fe^{2+} when exposed to the lysosome [94,95]. For the best design of a biocompatible coating, the coating should be able to be broken down into particles with diameters less than 5 nm allowing excretion through the renal system with minimal cytotoxicity [25]. By modifying the surface coating of the SPION to have a cationic surface, the cell labeling efficiency can also be increased compared to negatively charged or neutral surface coatings [49] (Figure 7b).

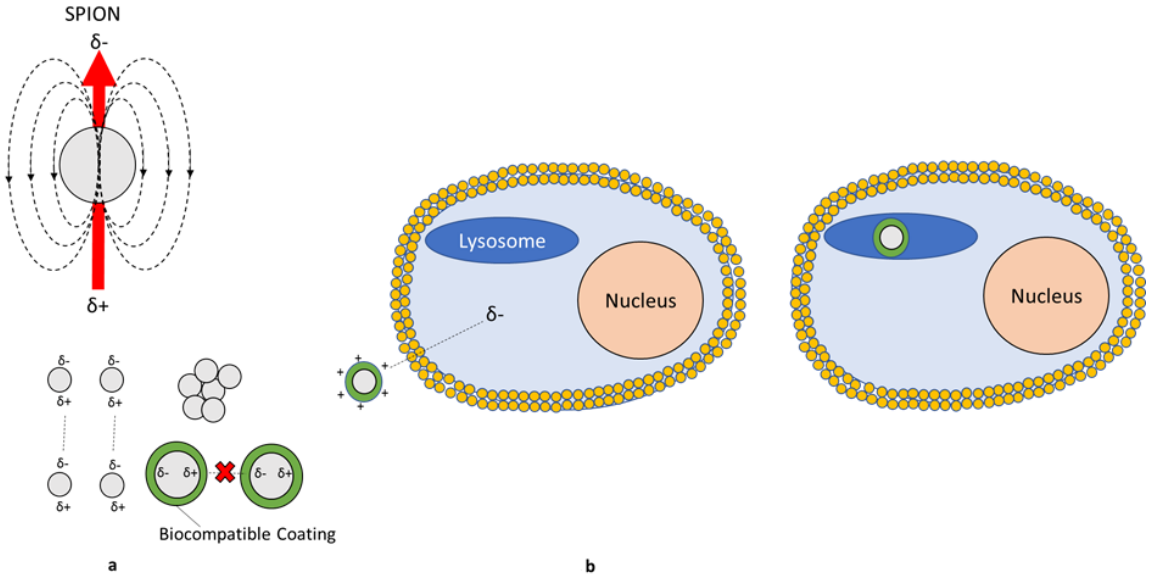

Figure 7. Pictorial diagram showing the ability of biocompatible coating of SPIONs to interfere with magnetic dipole-dipole induced agglutination of SPIONs (**a**) and encourage charge directed cell uptake with the delayed lysosomal release of free Fe^{2+} (**b**).

4.1. Dextran

Dextran is the coating used in the FDA approved Sinerem® and Endorem® SPIONs and has demonstrated great biocompatibility with no signs of inflammation or cytotoxicity at concentrations of 11.3 μg/mL [96]. Safety for the use of Dextran-coated SPIONs has been further demonstrated by the observation that Dextran is slowly degraded showing 89% excretion through the urine by 56 days, while the iron from the core of SPIONs enters the body iron stores before being incorporated into hemoglobin [97]. In addition to the great biocompatibility, Dextran-coated SPIONs have also shown versatility in their ability to target multiple different systems within the body. The use of Dextran-coated SPIONs is not limited to the selective imaging of macrophages in arthritic joints [23] but also can be functionalized to image human lymphocytes [98], myocardial infarct [99], tracking of T cells [100], and for the early detection of allograft chronic rejection [101].

4.2. Poly(ethylene)glycol (PEG)

Another common coating used to reduce interactions with cells or proteins and to neutralize the SPION surface is the hydrophilic and zwitterionic coating PEG, which has the advantage of the highest solubility and smallest HD among the common SPION coatings [54]. This allows PEG-coated SPIONs from 10 to 15 nm in diameter to become only 40 to 50 nm after PEGylation depending upon the molecular weight of PEG [18,102] while retaining the ability to provide strong T2 and T2* relaxation-based contrast in MR images [102]. While T2 is commonly referred to as "true" T2 and caused by atomic/molecular interactions, T2* is referred to as "observed" T2 and reflects true T2 as well as magnetic field inhomogeneities. The equation for T2* is (1/T2* = 1/T2true + 1/T2inhomogeneities). T2* weighted imaging uses certain MR sequences to accentuate local magnetic homogeneity effects to aid in the detection of deoxygenated hemoglobin, methemoglobin, or hemosiderin lesions in tissues [103]. This PEGylation effectively eliminates cytotoxicity as high as 1 mg/mL and provides protection against sedimentation for over two months at room temperature compared to only a week for uncoated SPIONs [18]. It was also shown that although the size of the SPION increases directly as the weight of the PEG increases from 1900 Da to 20,000 Da, the blood circulation time increased as well [104]. Further supporting the importance of coating material, it was also found that when the size of IONPs was less than 40 nm, the coating material had a stronger effect on biodistribution and blood half-life than the particle size [105]. Additional evidence of the protective effects of PEGylation was

demonstrated by the ability of the 23 nm PEGylated SPION incubated in mouse serum to retain 75% of 69Ge within the iron oxide core for 24 h compared to less than 60% retention in 6 h of the 10 nm uncoated SPIONs [106]. However, caution should still be taken to limit the size of SPIONs coated with PEG. When the size of the PEGylated SPIONs was increased as far as 129.3 nm and attached with positive or negatively charged functionalization groups, an increase in inflammatory biomarkers, lipid peroxidation, and DNA damage was seen compared to the control mice [107]. SPIONS can be clustered together within a single PEG coating to become PEG-SPION nanoclusters with superior MRI contrast results and saturation magnetization values of 44.4 emu/g compared to 2.4 emu/g for the clinically approved SPION Resovist [108]. These PEG-SPION nanoclusters were able to provide the same r2 relaxivity of Resovist at one-tenth of the concentration of Resovist [108].

4.3. Silica

The use of silica for SPION coating has also demonstrated great capabilities due to the biocompatibility, low cost, and tolerance of a wide range of pHs [109,110]. The protective effects of silica have been demonstrated by a fewer number of Fe^{3+} ions released from SPIONs and a slower metabolism and excretion rate of SPIONs, while at the same time not reducing the rate of uptake [94]. Porous silica gel encapsulations provide intimate contact between the water molecules and the iron oxide core for enhancement of MRI contrast while eliminating the toxicity of SPIONs and providing a framework for attaching many different types of ligands to SPIONs such as ^{64}Cu and ^{111}In for PET imaging [111]. The silica shell may be even further functionalized to increase endocytosis by binding Cu^{2+} to the surface of clustered SPIONs in silica to make the surface charge less negative, but this also results in a lower r2 value and T2 contrast strength via MRI [49]. This causes the SPION relaxivity to become inferior to the relaxivity value provided by the dextran-coated and clinically used Feridex nanoparticles [49]. To offset this decrease in relaxivity value and match Feridex, multiple SPIONs may be clustered within a single silica shell to increase both the relaxivity value and effective size of the particle [49].

4.4. Polyvinyl Alcohol (PVA)

Polyvinyl alcohol (PVA) coatings for SPIONs are unique due to the availability of amino or carboxyl groups to both regulate the charge of the coating as well as provide a point of attachment for peptides, proteins, antibodies, fluorescent dyes, and drugs [112] (Figure 8). By coating 14 nm SPIONs with PVA, a small aggregation of SPIONs forms inside the coating and the hydrodynamic size increases to 45 nm [113]. A study examining the cytotoxicity found that while the low dose of 6 μg of Fe per mouse knee did not induce an immune response when the concentration injected of PVA-coated SPION is as high as 24 μg of Fe per mouse knee, an acute inflammatory response marked by the upregulation of IL-1β, IL-6 and KC was seen [24]. However, this response was more severe in naïve mice compared to arthritic mice and decreased after two days with no significant cytotoxicity seen up to 14 days after injection [24]. Interestingly, this inflammatory response decreased when the injection was given locally vs. intravenously and the injection of PVA alone provoked a short-term inflammatory response that was more severe than the response from the PVA-coated SPION [24].

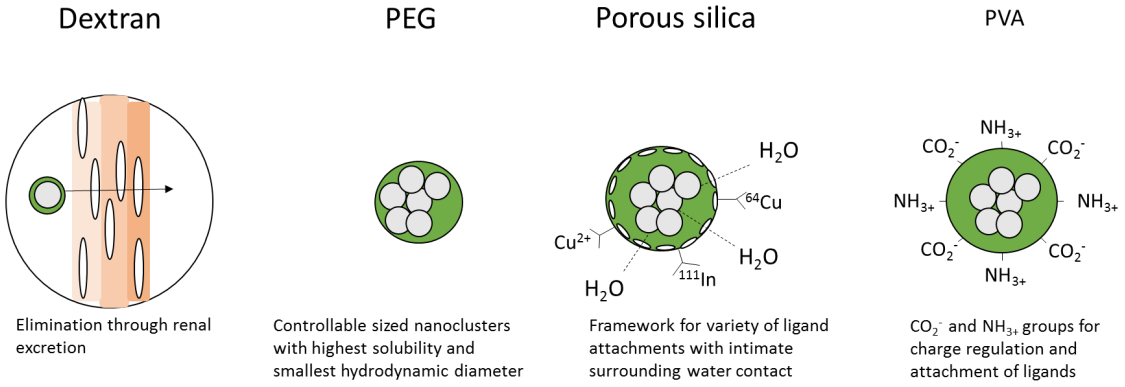

Figure 8. Pictorial diagram showing different coating of SPIONs.

4.5. Lipids

Researchers have also made developments in using lipids as coatings of SPIONs. The two different types of lipid-coatings are supported by lipid bilayers (SLBs) and hybrid lipid bilayers (HLBs) [114]. SLBs include an identical hydrophilic outer and inner surface of the lipid bilayer, which can be created by simply mixing the NPs with lipid vesicles such as 1,2-dioleoyl-sn-glycero-3-phosphocholine (DOPC), 1-palmitoyl-2-oleoyl-glycero-3-phosphocholine (POPC), or 1,2-miristoyl-sn-glycero-3-phosphocholine (DMPC). To facilitate the vesicle fusion process, anionic phospholipid 1,2-dioleoyl-sn-glycero-3-phosphoserine (DOPS) or the cationic lipid DOTAP may be used to target the charged surface of previously silica-coated NPs [115–119]. The use of HLB initially involves a capping agent that interacts with the NP surface to halt the growth of the NP and prevent precipitation and aggregation, leading to uniform size and distribution of NPs. The outer surface of the NP-bound capping agent is typically hydrophobic allowing for solubility in non-polar solvents, replacement by another layer of molecules, or coating with another layer of amphiphilic molecules [114]. Capping agents that have been used include oleylamine and oleic acid [120], as well as thiol, carboxyl, and amino-functional groups [121]. By adding a cyclohexane dispersion of SPIONs capped with oleylamine and oleic acid to an aqueous solution of lysophophatidycholine (LPC) molecules and sonicating at 50 °C to evaporate the organic solvent, an HLB with an inner leaflet of oleylamine and oleic acid and an outer leaflet of LPC may be formed on the SPION surface [122]. The avoidance of SPION aggregation was best demonstrated by using the 18LPC which had the lowest critical micelle concentration. Lipid coating of NPs gives the advantage of increased penetration of cell membranes, which is strongly dependent on the cholesterol content of the cell membrane, while not disturbing the overall membrane structure [123]. They also demonstrate high biocompatibility [124,125], enhanced MRI signal [126], and only a small increase in NP size as the typical thickness of the NP coating is only 2–6 nm depending on the length of lipids and capping agents used [114].

SPIONs have also been formulated with a lipid coating by first encapsulating within a silica shell and then mixing with 1,2-dipalmitoyl-sn-glycero-3-phosphocholine/cholesterol (DPPC/Ch). This significantly reduced the saturation magnetization values compared to the bare SPIONs from 64 emu g^{-1} to 5 emu g^{-1} and increased the size from 5–20 nm for bare SPIONs to 200 nm for silica and lipid-coated SPIONs [127]. However, this coating significantly reduced SPION toxicity by increasing cell viability from <70% to 87% and allowed for the multimodal therapeutic use of SPIONs, which will be discussed in further detail [127].

4.6. Other Coatings

Other coatings used to enhance the biocompatibility of nanoparticles as well as enhance their functionality come from a variety of compounds (Table 1). The use of chitosan oligosaccharide as a coating increases hydrophilicity and biocompatibility to reduce cytotoxicity, ROS production, and degradation of SPION, resulting in a slower release of iron ions [128]. Other hydrophilic coatings that

can be used to avoid uptake by the RES to remain in the blood circulation for a prolonged amount of time are Pluronic [129] and the surfactant Tween 80 which showed no cytotoxicity for 30 nm SPIONs at a concentration of 100 μg/mL for 6 h of exposure [59]. If a hydrophilic coating of the nanoparticle is not able to be accomplished, another approach is to confine the iron oxide core within a cage. While fullerene cages have been used to confine the traditional MRI contrast agent gadolinium [130], gold nanocages present the ability to confine particles that are larger than 1 nm. Gold nanocages with inert nature, extreme resistance to oxidation, and considerable biocompatibility are able to be produced in sizes similar to SPIONs with diameters consisting of 40 nm and a wall thickness of 3.3 nm [131]. Another approach to mitigate the effects of cytotoxicity instead of reducing the leeching of iron ions is to coat IONPs with poly (Trolox ester) to counteract the pro-oxidant effects of IONPs [132]. It is also important to consider the effects that the coating has on IONP uptake in specific areas of the body. It was shown that while albumin, lecithin, PEG, polysorbital 80, or peptide attachments can enhance nanoparticle uptake into cells, PEG interferes in nanoparticle uptake in the liver [133]. While some groups have focused on using oleic acid as a biocompatible coating for SPIONs, it was shown to be rapidly removed from the core by the differing biodistribution of radioactivity within the body after labeling the oleic acid with ^{14}C and the core with ^{59}Fe [134].

Table 1. List of commonly used SPION coating materials, their sizes, and properties.

SPION Coating	Size/Concentration	Additional Properties
Dextran	150 nm-Endorem® 30 nm-Sinerem® at 11.3 μg/mL	89% renal excretion by 56 days, can add amine to dextran for attachment of ^{18}F for PET imaging
Poly(ethylene)glycol (PEG)	50nm SPIONs at 1 mg/mL	Highest solubility and smallest hydrodynamic diameter, can attach folic acid to target upregulated receptors in cancerous tissue, can attach ^{68}Ga for PET imaging by mixing with $[^{68}Ga]GaCl_3$
Polyvinyl alcohol (PVA)	45 nm SPIONs at 6 μg of Fe per mouse knee	Available amino or carboxyl groups to both regulate the charge of the coating as well as provide a point of attachment for peptides, proteins, antibodies, fluorescent dyes, and drugs. Can apply magnetic hyperthermia treatment to release attachments from heat-labile PVA coating. Specific uptake in arthritic joints
Silica	4–33 nm	Provides a framework for the attachment of a variety of ligands such as ^{64}Cu and ^{111}In for PET and SPECT imaging respectively, Cu^{2+} to enhance endocytosis. Low cost and tolerant of a broad range of pH
Oleic acid	10 nm	Rapidly removed from IONP core
Oleic acid-Pluronic	10 nm SPIONs at 100 μg/mL	Prevents removal of oleic acid and allows for loading of water-insoluble drugs onto IONP surface
Tween 80	30 nm SPIONs at 100 μg/mL for 6 h	Hydrophilic, avoids uptake by RES to give prolonged half-life
Gold nanocages	40 nm	Inert nature, extreme resistance to oxidation, absorbs external near-infrared light
Chitosan	50 nm	Biocompatible and biodegradable surface, allows conjugation with TMZ and chlorotoxin

5. Hybrid Use of SPIONs

5.1. Targeting of SPIONs

While SPIONs have been shown to passively target cancerous tissue via the EPR effect, SPIONs may be further functionalized by attaching targeting ligands to the NP surface that recognize biological structures that are overexpressed or unique to cancer cells [25]. This allows the targeting and T2 contrast of prostate cancer cells via a SPION conjugated deimmunized mouse monoclonal antibody (muJ591) that targets a specific prostate biomarker [135]. Epithelial cancer may also be targeted by SPIONs by seeking the epidermal growth factor [136] and magnetic targeting alone can use an external magnetic field to draw SPIONs to the site of interest [137]. Additionally, many cancers overexpress folate receptors that are absent in normal cells [138]. Folic-acid-coated SPIONs can then be used to target the folate receptors [138] (Figure 9) and lead to accumulations of SPIONs up to 50% of the injected dose/gram of tissue in the tumor when SPIONs from 7–9 nm were clustered into sizes of 60–100 nm before being PEGylated with folic acid also exposed on the surface [108]. Interestingly, these folic-acid-PEGylated SPION nanoclusters also showed the ability to specifically concentrate on the cancerous tissues and not the necrotic tissues within the tumor [108].

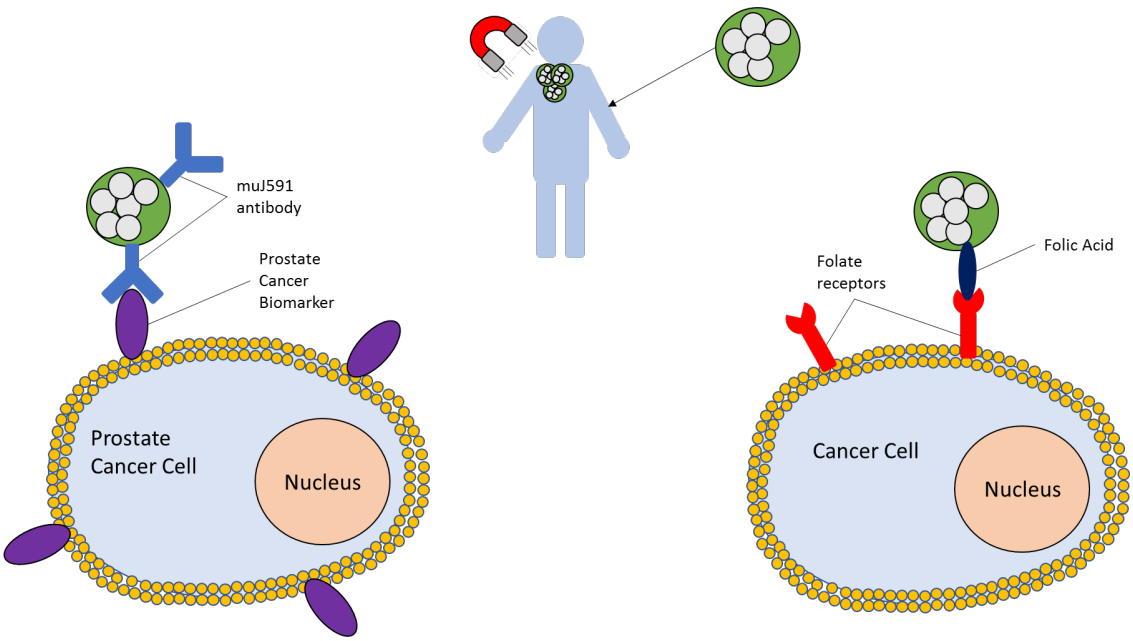

Figure 9. Pictorial diagram showing targeted delivery of SPIONs.

5.2. Magnetic Hyperthermia Treatment

A unique property of SPIONs is that they heat due to hysteresis loss, Néel relaxation, and induced eddy currents when exposed to an external magnetic field at a specific frequency [139]. Magnetic hyperthermia treatment (MHT) is when external magnetic fields are applied to SPIONs within the body to raise the temperature of the cells surrounding the SPIONs. If the temperature of the surrounding cells rises above 42 °C, the structural and functional proteins within cells are disrupted resulting in necrosis [140,141] and the resistance of tumor growth [142]. The increase in temperature following MHT is often highest in the interstitial extracellular space allowing for increased drug penetration via the damaged extracellular matrix, while the temperature inside of the cells does not increase as much [142] (Figure 10). When used for cancer treatment, MHT is also able to take advantage of the property that tumors are more highly susceptible to heat compared to normal tissue and that the amount of heat produced via MHT can be altered by adjusting the strength of the alternating current (AC) magnetic field [108]. These properties of MHT are attractive and have shown success in treating

multiple types of cancer such as prostate cancer [143,144], glioblastoma [145], and metastatic bone tumors [146]. It is important to note, however, that to avoid damage to healthy tissues a safe level of AC magnetic field for MHT should be used where the product of the amplitude and frequency is less than 5×109 Am^{-1} s^{-1} [147,148]. To avoid damage to surrounding tissues, it is also recommended for SPIONs to have a homogenous distribution to allow for a uniform temperature within the tumor tissues [25].

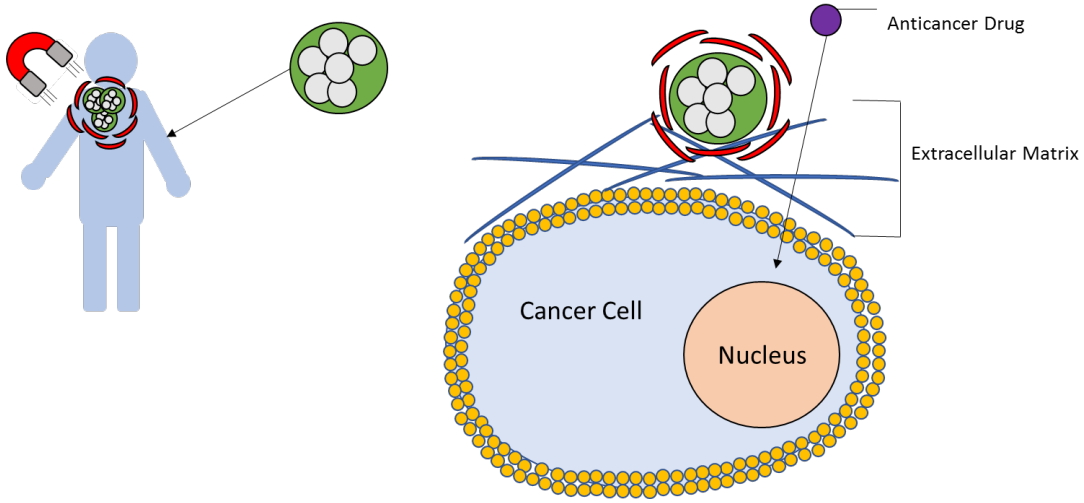

Figure 10. Pictorial diagram showing the use of SPION for the magnetic hyperthermia treatment approach.

The struggles of using MHT for in vivo treatment have arisen due to the fact that SPIONs only show superparamagnetism when they are less than 10 nm and at that size, they leak from the pores in fenestrated capillaries without accumulating in tumors [108]. To solve this problem, researchers have clustered 7–9 nm SPIONs together within a single coating of PEG-Folic acid to have an overall diameter from 60–100 nm, which allows for the EPR effect as well as an increased relaxivity and specific absorption rate for MHT [108]. Aggregation of the clustered SPIONs was seen up to 323 nm in size if they were allowed to remain undisturbed for three months, but the aggregates of clustered SPIONs uniformly redispersed following ultrasonic treatment [108]. These clustered SPIONs selectivity accumulated within the cancerous tissue and not the necrotic tissue within the tumor to bring the temperature of the tumor 6 °C higher than the surrounding tissues after 20 min of MHT [108]. It is important to note that the rise in temperature at equal levels of AC magnetic field is dramatically reduced following MHT for in vivo studies compared to in vitro studies, likely due to the thermal diffusion via blood flow [108]. When following up with the MHT treated mice with tumors 35 days after treatment, the tumor volume of the MHT group was only one-tenth of the tumor volume for the control group and the MHT group mice survived past 12 weeks, while the control mice only survived up to eight weeks [108]. The researchers concluded that while these clustered SPIONs are larger in size, they are still biodegradable and able to be excreted via the urine or feces since about 6% of the injected dose/g was ultimately not found in any organs at 24 h postinjection [108]. When examining the heating during MHT for the lipid/silica-coated NPs, the temperature reached only 32 °C after 10 min of exposure to the AC field and took 45 min to reach 43 °C compared to the uncoated NPs reaching 43 °C within 5 min. This was likely due to the decreased saturation magnetization values seen in the lipid/silica-coated NPs as the heat generated during MHT is proportional to the total area of hysteresis [127].

SPIONs have also been modified by attaching the monoclonal antibody trastuzumab (Tmab) to target HER2 receptors in breast cancer. This conjugation reaction had an efficiency of around 54.6% by mass and the SPION-Tmab showed greater activity against SKOV-3 cells than trastuzumab alone. These SPIONs were able to be further modified by doping the core with holmium^{3+} at a

concentration of 1% atomic versus total iron content to preserve the structural and magnetic properties of SPIONs. This doping of holmium allows for endoradiotherapy via soft, beta(−) radiation when nonradioactive holmium is replaced with a radioactive ^{166}Holmium. These holmium-doped SPIONs presented with a similar saturation magnetization value of 72 emu/g compared to the undoped bulk magnetite. For the SPIONs to reach 45 °C the optimal frequencies for MHT were 345.5–487.75 kHz and the amplitudes were 150–200 G. Together these conjugates are designed to allow active targeting as well as simultaneous internal localized irradiation and MHT of specific cancers [149].

As discussed earlier, the upregulation of folate receptors in tumor cells can be used for targeted therapy by coating SPIONs with folic acid. Folic-acid-coated SPIONs have one moiety of the folic acid available for strong affinity with the folate receptor and another moiety that sticks out of the pocket entrance which may be functionalized with drugs or nanoparticles without adversely affecting the receptor binding. Folate-conjugated PEGylated SPIONs were formulated by first performing PEGylation and then mixing with folic acid. The size of these SPIONs was 109.7 nm and they demonstrated a saturation magnetization value of 73.1 emu g^{-1} compared to 92 emu g^{-1} for the uncoated SPIONs. The uncoated SPIONs reached a temperature of 42 °C in 80 s during MHT compared to 222 s for the folate conjugated PEGylated SPIONs [150].

5.3. Drug Loaded SPIONs

A large concern of current anticancer agents is that they demonstrate nonspecific toxicities that significantly limit their therapeutic potentials [129]. To provide a medium for hydrophobic anticancer drugs like Paclitaxel, they are commonly dissolved in a mixture of hydrogenated castor oils called Cremophor EL (BASF), which has been shown to cause a hypersensitivity reaction without providing adequate pharmacokinetics and drug distribution for effective tumor therapy [151,152]. While one group proposed that SPIONs alone may be able to treat tumors by exhibiting ROS promoting effects within tumor cells [19] other groups have proposed using SPIONs as a carrier vessel for anticancer drugs that can be directed from the blood circulation to the tumor site of interest by an external localized magnetic field gradient [129]. However, complications often arise when loading therapeutic agents to hydrophilic coatings due to the ionic bond formation that often involves multiple complex steps with only limited drug-loading capability [153]. Additionally, the need for chronic drug retention within the tumor for therapy is also problematic due to the observation that the drug often dissociates from the coating within hours [153]. Nevertheless, many groups have been able to navigate these problems to allow drug delivery via IONPs.

One approach to load the anticancer agent Doxorubicin (DOX) onto IONPs showed promise by loading the drug into the oleic acid (OA) coating of IONPs and binding the outer surface of OA with the hydrophobic polypropylene oxide region of Pluronic leaving the hydrophilic ends of Pluronic, known as polyethylene oxide, free to the outside environment to give aqueous dispersity to the particle [129] (Figure 11a). This mechanism of binding was supported by the absence of binding of Pluronic to IONP in the absence of oleic acid and an increase in Pluronic binding associated with a higher OA concentration [129]. Although the IONP required 23 wt % of OA to be dispersed in hexane, it was shown that only 17 wt % binds to the IONP via the carboxylic acid group of OA and that any additional wt % of OA forms a multilayer coating [129]. After optimizing the concentrations of reagents to 70.1 wt % iron oxide, 15.4 wt % OA, and 14.5 wt % Pluronic, the loading efficiency of DOX became as high as 82% [129]. This formulation allowed the slow distribution of DOX to the outside environment by releasing 28% in two days and 62% of DOX by one week [129]. These DOX-loaded IONPs showed the ability of DOX to enter MCF-7 cells within 2 h and retention of DOX in the nucleus at 24 and 48 h of incubation [129]. Further evidence of the robustness of this method to deliver water-insoluble drugs was that the dose-dependent cytotoxicity was lower than that of pure DOX, no change in magnetization properties was observed compared to the naked IONP, and that this method worked to load Paclitaxel as well [129].

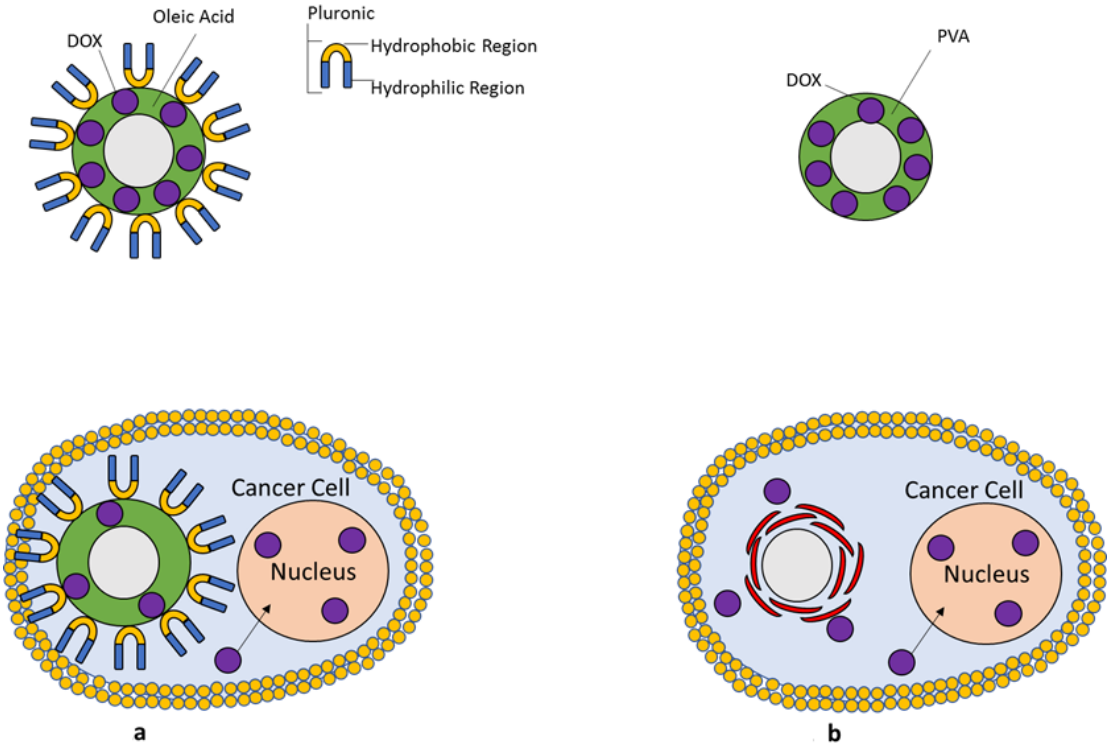

Figure 11. Pictorial diagram showing drug-loaded SPIONs for chemotherapeutic application using Pluronic coating for slowed release (**a**) or PVA with magnetic hyperthermia treatment for controlled release (**b**).

Another group has also developed a method to allow therapeutics that are hydrophobic or nonspecific in targeting cells or tissues to be shielded and transported to the desired site via either an external magnetic field, the EPR effect, or by attaching ligands to the surface of the heat-labile PVA-coated SPIONs [25]. Once the SPIONs are confirmed to be within the desired tissue site via MRI, 50 kHz MHT can be applied to release the drugs from the PVA coating [154] (Figure 11b). An advantage of this method is that the amount of drug delivery can also be measured in vivo via MRI by the difference in T1 and T2 values for the drug-loaded and drug-released state of SPIONs since the drugs Flutax1, DOX, and DiR all cause an increase in T1 and T2 values in a linear response due to the interference of water diffusion to the iron oxide cores [155].

Lipid-coated NPs may also be further functionalized by including PEG chains in the lipid coating to improve colloidal stability as well as provide a conjugation site for peptides, antibodies [156,157], chemotherapeutic drugs for pancreatic ductal adenocarcinoma [158], near-infrared fluorescence agent and hepatocyte targeting polymer [159], and TLR4 agonists [160]. The thermoresponsive phospholipid 1,2-dipalmitoyl-sn-glycero-3-phosphocholine (DPPC) may also be used as an anticancer delivery vector for NPs as it transitions from the gel to liquid phase at 41 °C [161–163]. When comparing an uncoated SPION loaded with Doxorubicin (DOX) to a lipid/silica-coated and DOX-loaded SPION, a significant decrease in cytotoxicity was observed as cell viability increased from 36% to 73%. The entrapment efficiency when loading DOX to these lipid/silica-coated SPIONs was found to be 58% after 48 h [127].

5.4. Biotherapeutics

While delivering chemotherapy drugs demonstrates a unique use for SPIONs, they are also capable of carrying and delivering biological agents. This is known as biotherapeutic therapy and the agents delivered by SPIONs can be DNA to replace the mutated genes, small interfering RNA (siRNA) to disrupt protein expression of those genes, or proteins and peptides to disrupt specific cell mechanisms like cell adhesion or angiogenesis to ultimately cause the cell to enter apoptosis [164].

While only limited success has been achieved in the past due to immunogenicity induced by the delivery vectors of biotherapeutics [164], modifications of SPIONs to include biocompatible coatings have prompted recent success. By conjugating the DNA alkylating agent used to treat glioblastoma known as TMZ [165] and the tumor-targeting peptide chlorotoxin to a chitosan coating layer around IONP, both greater stability compared to naked TMZ was achieved and a two to six-fold increase in uptake by glioblastoma cells was seen compared to unconjugated IONPs [166]. When loading DNA or siRNA onto a SPION, they can be directly bound to a positively charged polymer coating through the negatively charged nucleic acids [167] and covered with a coating such as polyethylimine (PEI) that will both protect the DNA or siRNA while in transit outside of the cell and release the agents due to the cleaving of the disulfide crosslinking of PEI via glutathione once the SPION enters the cell [168] (Figure 12). Since DNA and siRNA need to access the nucleus of a cell to induce a cell response, peptides must also be attached to the surface of SPIONs to facilitate nuclear localization. Together these conditions demonstrated the biotherapeutic abilities of IONPs by coating IONPs with chitosan, siRNA-loaded PEI, and PEG layer to ultimately cause the tumor cell to become more susceptible to γ-rays after the delivery of siRNA has suppressed the radiation-resistant DNA repair protein [169].

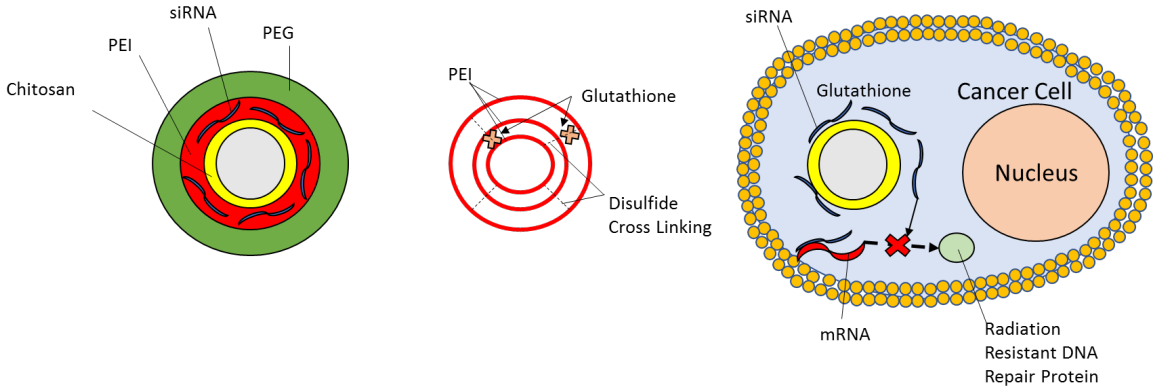

Figure 12. Pictorial diagram showing the use of SPION for biotherapeutic siRNA therapy approach.

Other approaches to use IONPs as a treatment for cancerous tissues include photothermal ablation and photodynamic therapy. Photothermal ablation is when light is absorbed by NPs and then converted to thermal energy to cause cell death in the vicinity, while photodynamic therapy is when photosensitizing agents are attached to NPs and activated by a specific wavelength of an external light source to create singlet oxygen species to cause irreversible free radical damage within 20 nm of the NP [170]. These photosensitizing agents for photodynamic therapy often make use of the natural property of gold to absorb the near-infrared (NIR) wavelengths that demonstrate deep tissue penetration [171]. By using a gold shell to absorb the external NIR light source and by attaching a specific antibody that targets colorectal cancer cells for five times faster internalization of IONPs, photothermal therapy was used to destroy 53% of A33-expressing cells within 6 min of exposure to 800 nm laser radiation at 5.1 W cm^{-2} [172].

5.5. Multi-Modal Imaging Probes

A large limitation of using MRI is that MRI studies alone cannot provide in vivo quantification due to possible agglomeration and an increase of hydrodynamic diameters caused by opsonization, which makes it difficult to determine the correlation of relaxivities to local particle concentration [173,174]. In addition to this, the low sensitivity of MRI is often insufficient for detecting tissue injury, assessment of tissue/organ function, and tracking implanted stem cells [49]. While the use of SPIONs still cannot provide quantitative distribution data via MRI [134], SPIONs present the opportunity to perform multiple imaging techniques either in succession or simultaneously by strategically supplementing the disadvantages of one imaging technique with the advantages of another. Of the common imaging

techniques, MRI is known to have great spatial resolution and poor sensitivity [25]. While CT presents with similar strengths and weaknesses compared to MRI, the ability of SPION to act as a dual MRI contrast and CT X-ray attenuating agent has been demonstrated by incorporating bismuth into the core of SPIONs [90].

The advantage of using optical imaging is the inexpensiveness and high sensitivity, but this technique is not able to penetrate through deep tissues due to the scattering of light [25]. During optical imaging, fluorescent probes that are conjugated to SPIONs can absorb an external light source and return photons at a longer wavelength and lower energy to the external detector [175]. This approach is attractive for surgeons operating on cancerous tissue as it allows SPIONs to provide both anatomical information before surgery via MRI and molecular detail during surgery via fluorescence imaging [176,177]. To help maximize the tissue penetration of optical imaging, the NIR light absorbing and emitting Cy5.5 can be conjugated to SPIONs [178], but positron emission tomography (PET) still offers greater tissue penetration power (Figure 13).

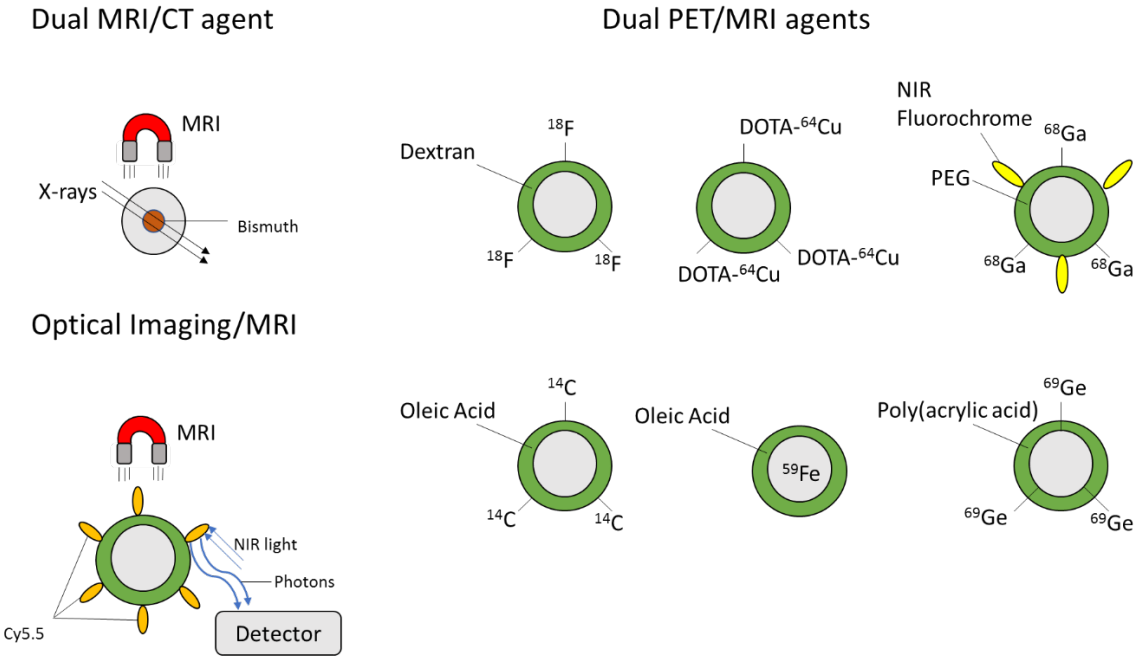

Figure 13. Pictorial diagram showing the use of SPION as a multi-modal imaging probe.

While CT does not pair well with MRI because it contains the same strengths and weaknesses, positron emission tomography (PET) with high sensitivity and no structural information supplements MRI extremely well [25]. SPION-PET nanoprobes can take advantage of the hybrid PET/MRI cameras that are already in clinical use [17] and have been established by incorporating a variety of positron-emitting isotopes including ^{18}F, ^{14}C, ^{64}Cu, ^{68}Ga, ^{59}Fe, and ^{69}Ge (Figure 13). To conjugate the widely produced and available ^{18}F isotope to SPIONs, ^{18}F was transferred from [^{18}F]F-PEG to a free azide available on the aminated cross-linked dextran iron oxide nanoparticle [179]. This allowed for the detection threshold to be reached via PET-CT imaging at a SPION concentration that was 200 times lower than what MRI alone could achieve [179]. Instead of using an azide to facilitate conjugation of a positron-emitting radioisotope to SPION, DOTA can also be used to chelate ^{64}Cu to enable PET and MRI imaging simultaneously [180]. These SPIONs were used to effectively track the biodistribution of primary T cells during T-cell therapy by taking advantage of the negatively charged cell membranes and the positive charge given to the SPIONs to promote internalization within 10 min while avoiding cytotoxicity and retaining T cell tumor-targeting capability [180]. It was also demonstrated that to minimize radiation damage to cells, the radioactivity of [^{64}Cu]Cu-SPIONs should be limited to 0.6mCi[182]. Another approach used ^{68}Ga by mixing PEG-coated SPION with [^{68}Ga]$GaCl_3$ at 50 °C for

15 min to achieve 97% radiolabeling efficiency, sensitive PET imaging, high-resolution MR imaging, and Cherenkov luminescence optical guided secondary lymph node surgery [17]. These [^{68}Ga]Ga-SPIONs showed high stability of up to 4 h in human serum while also demonstrating that their ability to remain in the secondary lymph node tissue for 25 h after injection [17].

Another radiolabeling option for SPIONs that has been explored is using [^{14}C]-oleic acid coating, but it was shown that the [^{14}C]-oleic acid is easily replaced in equilibrium with unlabeled oleic acid [181]. To ensure that the positron-emitting isotope remains bound to the SPION, these researchers have also incorporated a positron-emitting isotope into the core rather than the coating. By irradiating the iron within the core of the SPIO to create [^{59}Fe]Fe-SPIOs, the uptake of triglyceride-rich proteins was quantified in brown adipose tissue after mice exposure to 4 °C demonstrating a significant increase of ^{59}Fe in the brown adipose tissue [181]. A disadvantage of directly irradiating the iron oxide core of SPIONs to create ^{59}Fe, however, is that natural iron only contains 0.28% ^{58}Fe, creating a demand for long irradiation times and leading to a high potential for damage to the biocompatible coating surrounding the SPION [181]. A simple method of incorporating positron-emitting isotopes into the core of SPIONs is by simply mixing ^{69}Ge ions with poly(acrylic acid) (PAA) coated SPIONs at 37 °C and pH 7 to achieve a radiolabeling yield above 75% after 3 h [106]. Interestingly, it was also demonstrated that ^{69}Ge cannot bind to free PAA in solution while ^{69}Ge binds to naked SPIONs at a slightly higher rate than it does to PAA-coated SPIONs [106].

6. Summary

In spite of oxidative damage and cytotoxicity caused by uncoated SPIONs, the SPIONs hold considerable potential as a contrast agent for MRI, multimodal imaging probes, and target delivery of therapeutics including biotherapeutics and chemotherapy agents. Significant work has already been done but more work is needed to further advance the SPIONs to the next level like the use of SPIONs for targeted alpha radiotherapy (Ac-225 and Bi-212) and targeted delivery of stem cells and exosomes. To further elaborate the targeted delivery approach, SPIONs should continue to be developed to provide a framework for the attachment of a variety of monoclonal antibodies and biological agents. The frequent use of next-generation sequencing in the clinical practice to test for gene mutations present in the cancer tissue including ALK1, BRAF, BRCA1/2, EGFR, Kit (CD117), ROS1, HER2, PD-L1, 17p deletion, BCR-ABL1, F1P1L1-PDGFRA, PDGFR, and PML/RAR [182] can be extended to SPIONs via including monoclonal antibodies and kinase inhibitors specific to these gene mutations. Some of these antibodies and kinase inhibitors have already been developed, which presents the opportunity to use the results of this test to guide biologic therapy based on the specific susceptibility reported in the tumor [182]. If a SPION coating is developed that allows for easy integration of a variety of monoclonal antibodies and kinase inhibitors, SPION therapy may be directed towards the specific gene mutations that are present in the tissue by coating with the appropriate biologic agent. If the biologic-agent-coated SPION can be further loaded with chemotherapeutic agents, the SPION may theoretically be directed via the biologic agent to the cancer tissue where MHT or other mechanisms can assist in the controlled release of chemotherapeutic agents that would otherwise present with nonspecific toxicity.

Funding: Authors would like to thank the Department of Radiology Mayo Clinic Rochester for financial support.

Conflicts of Interest: The authors declare no conflict of interest.

References

1. Eryaman, Y.; Zhang, P.; Utecht, L.; Kose, K.; Lagore, R.L.; DelaBarre, L.; Kulesa, J.; Eberly, L.E.; Adriany, G.; Iles, T.L.; et al. Investigating the physiological effects of 10.5 Tesla static field exposure on anesthetized swine. *Magn. Reson. Med.* **2018**, *79*, 511–514. [CrossRef] [PubMed]
2. Kandasamy, G.; Maity, D. Recent advances in superparamagnetic iron oxide nanoparticles (SPIONs) for in vitro and in vivo cancer nanotheranostics. *Int. J. Pharm.* **2015**, *496*, 191–218. [CrossRef] [PubMed]

3. Khurana, A.; Runge, V.M.; Narayanan, M.; Greene, J.F.; Nickel, A.E. Nephrogenic systemic fibrosis: A review of 6 cases temporally related to gadodiamide injection (Omniscan). *Investig. Radiol.* **2007**, *42*, 139–145. [CrossRef] [PubMed]
4. Edward, M.; Quinn, J.A.; Mukherjee, S.; Jensen, M.B.V.; Jardine, A.G.; Mark, P.B.; Burden, A.D. Gadodiamide contrast agent "activates" fibroblasts: A possible cause of nephrogenic systemic fibrosis. *J. Pathol.* **2008**, *214*, 584–593. [CrossRef]
5. Runge, V.M. Dechelation (Transmetalation): Consequences and Safety Concerns with the Linear Gadolinium-Based Contrast Agents, in View of Recent Health Care Rulings by the EMA (Europe), FDA (United States), and PMDA (Japan). *Investig. Radiol.* **2018**, *53*, 571–578. [CrossRef]
6. Radbruch, A.; Weberling, L.D.; Kieslich, P.J.; Eidel, O.; Burth, S.; Kickingereder, P.; Heiland, S.; Wick, W.; Schlemmer, H.P.; Bendszus, M. Gadolinium retention in the dentate nucleus and globus pallidus is dependent on the class of contrast agent. *Radiology* **2015**, *275*, 783–791. [CrossRef]
7. Kanda, T.; Ishii, K.; Kawaguchi, H.; Kitajima, K.; Takenaka, D. High signal intensity in the dentate nucleus and globus pallidus on unenhanced T1-weighted MR images: Relationship with increasing cumulative dose of a gadoliniumbased contrast material. *Radiology* **2014**, *270*, 834–841. [CrossRef]
8. Kanda, T.; Fukusato, T.; Matsuda, M.; Toyoda, K.; Oba, H.; Kotoku, J.; Haruyama, T.; Kitajima, K.; Furui, S. Gadolinium-based contrast agent accumulates in the brain even in subjects without severe renal dysfunction: Evaluation of autopsy brain specimens with inductively coupled plasma mass spectroscopy. *Radiology* **2015**, *276*, 228–232. [CrossRef]
9. Kanda, T.; Osawa, M.; Oba, H.; Toyoda, K.; Kotoku, J.; Haruyama, T.; Takeshita, K.; Furui, S. High signal intensity in dentate nucleus on unenhanced T1-weighted MR images: Association with linear versus macrocyclic gadolinium chelate administration. *Radiology* **2015**, *275*, 803–809. [CrossRef]
10. McDonald, R.J.; McDonald, J.S.; Dai, D.; Schroeder, D.; Jentoft, M.E.; Murray, D.L.; Kadirvel, R.; Eckel, L.J.; Kallmes, D.F. Comparison of gadolinium concentrations within multiple rat organs after intravenous administration of linear versus macrocyclic gadolinium chelates. *Radiology* **2017**, *285*, 536–545. [CrossRef]
11. Lord, M.L.; Chettle, D.R.; Gräfe, J.L.; Noseworthy, M.D.; McNeill, F.E. Observed deposition of gadolinium in bone using a new noninvasive in vivo biomedical device: Results of a small pilot feasibility study. *Radiology* **2018**, *287*, 96–103. [CrossRef] [PubMed]
12. Kartamihardja, A.A.P.; Nakajima, T.; Kameo, S.; Koyama, H.; Tsushima, Y. Impact of Impaired Renal Function on Gadolinium Retention after Administration of Gadolinium-Based Contrast Agents in a Mouse Model. *Investig. Radiol.* **2016**, *51*, 655–660. [CrossRef] [PubMed]
13. Harvey, H.B.; Gowda, V.; Cheng, G. Gadolinium Deposition Disease: A New Risk Management Threat. *J. Am. Coll. Radiol.* **2020**, *17*, 546–550. [CrossRef] [PubMed]
14. Pan, D.; Schmieder, A.H.; Wickline, S.A.; Lanza, G.M. Manganese-based MRI contrast agents: Past, present, and future. *Tetrahedron* **2011**, *67*, 8431–8444. [CrossRef]
15. Weissleder, R.; Stark, D.D.; Engelstad, B.L.; Bacon, B.R.; Compton, C.C.; White, D.L.; Jacobs, P.; Lewis, J. Superparamagnetic iron oxide: Pharmacokinetics and toxicity. *Am. J. Roentgenol.* **1989**, *152*, 167–173. [CrossRef]
16. Kehagias, D.T.; Gouliamos, A.D.; Smyrniotis, V.; Vlahos, L.J. Diagnostic efficacy and safety of MRI of the liver with superparamagnetic iron oxide particles (SH U 555 A). *J. Magn. Reson. Imaging* **2001**, *14*, 595–601. [CrossRef]
17. Madru, R.; Tran, T.A.; Axelsson, J.; Ingvar, C.; Bibic, A.; Ståhlberg, F.; Knutsson, L.; Strand, S.-E. (68)Ga-labeled superparamagnetic iron oxide nanoparticles (SPIONs) for multi-modality PET/MR/Cherenkov luminescence imaging of sentinel lymph nodes. *Am. J. Nucl. Med. Mol. Imaging* **2013**, *4*, 60–69.
18. Gupta, A.K.; Wells, S. Surface-Modified Superparamagnetic Nanoparticles for Drug Delivery: Preparation, Characterization, and Cytotoxicity Studies. *IEEE Trans. Nanobiosci.* **2004**, *3*, 66–73. [CrossRef]
19. Kuchma, E.A.; Zolotukhin, P.V.; Belanova, A.A.; Soldatov, M.A.; Lastovina, T.A.; Kubrin, S.P.; Nikolsky, A.V.; Mirmikova, L.I.; Soldatov, A.V. Low toxic maghemite nanoparticles for theranostic applications. *Int. J. Nanomed.* **2017**, *12*, 6365–6371. [CrossRef]
20. Smolensky, E.D.; Park, H.Y.E.; Zhou, Y.; Rolla, G.A.; Marjańska, M.; Botta, M.; Pierre, V.C. Scaling laws at the nanosize: The effect of particle size and shape on the magnetism and relaxivity of iron oxide nanoparticle contrast agents. *J. Mater. Chem. B* **2013**, *1*, 2818–2828. [CrossRef]

21. Jun, Y.W.; Huh, Y.M.; Choi, J.S.; Lee, J.H.; Song, H.T.; Kim, S.; Yoon, S.; Kim, K.S.; Shin, J.S.; Suh, J.S.; et al. Nanoscale Size Effect of Magnetic Nanocrystals and Their Utilization for Cancer Diagnosis via Magnetic Resonance Imaging. *J. Am. Chem. Soc.* **2005**, *127*, 5732–5733. [CrossRef] [PubMed]
22. Tromsdorf, U.I.; Bruns, O.T.; Salmen, S.C.; Beisiegel, U.; Weller, H. A highly effective, nontoxic T1 MR contrast agent based on ultrasmall PEGylated iron oxide nanoparticles. *Nano Lett.* **2009**, *9*, 4434–4440. [CrossRef] [PubMed]
23. Beckmann, N.; Falk, R.; Zurbrügg, S.; Dawson, J.; Engelhardt, P. Macrophage infiltration into the rat knee detected by MRI in a model of antigen-induced arthritis. *Magn. Reson. Med.* **2003**, *49*, 1047–1055. [CrossRef] [PubMed]
24. Vermeij, E.A.; Koenders, M.I.; Bennink, M.B.; Crowe, L.A.; Maurizi, L.; Vallée, J.P.; Hofmann, H.; Van Den Berg, W.B.; Van Lent, P.L.E.M.; Van De Loo, F.A.J. The in-vivo use of superparamagnetic iron oxide nanoparticles to detect inflammation elicits a cytokine response but does not aggravate experimental arthritis. *PLoS ONE* **2015**, *10*, e0126687. [CrossRef] [PubMed]
25. Revia, R.A.; Zhang, M. Magnetite nanoparticles for cancer diagnosis, treatment, and treatment monitoring: Recent advances. *Mater. Today* **2016**, *19*, 157–168. [CrossRef]
26. Peer, D.; Karp, J.M.; Hong, S.; Farokhzad, O.C.; Margalit, R.; Langer, R. Nanocarriers as an emerging platform for cancer therapy. *Nat. Nanotechnol.* **2007**, *2*, 751–760. [CrossRef]
27. Zhang, J.; Lou, X.; Jin, L.; Zhou, R.; Liu, S.; Xu, N.; Liao, D.J. Necrosis, and then stress induced necrosis-like cell death, but not apoptosis, should be the preferred cell death mode for chemotherapy: Clearance of a few misconceptions. *Oncoscience* **2014**, *1*, 407–422. [CrossRef]
28. Corot, C.; Robert, P.; Idée, J.M.; Port, M. Recent advances in iron oxide nanocrystal technology for medical imaging. *Adv. Drug Deliv. Rev.* **2006**, *58*, 1471–1504. [CrossRef]
29. Donaldson, K.; Schinwald, A.; Murphy, F.; Cho, W.S.; Duffin, R.; Tran, L.; Poland, C. The biologically effective dose in inhalation nanotoxicology. *Acc. Chem. Res.* **2013**, *46*, 723–732. [CrossRef]
30. Galaris, D.; Pantopoulos, K. Oxidative stress and iron homeostasis: Mechanistic and health aspects. *Crit. Rev. Clin. Lab. Sci.* **2008**, *45*, 1–23. [CrossRef]
31. Halliwell, B.; Gutteridge, J.M.C. *Free Radicals in Biology and Medicine*, 2nd ed.; Oxford University Press: New York, NY, USA, 1991; Volume 10, ISBN 0198500440.
32. Nel, A. Air pollution-related illness: Effects of particles. *Science* **2005**, *308*, 804–806. [CrossRef] [PubMed]
33. Bell, A.T. The impact of nanoscience on heterogeneous catalysis. *Science* **2003**, *299*, 1688–1691. [CrossRef] [PubMed]
34. Xiao, G.G.; Wang, M.; Li, N.; Loo, J.A.; Nel, A.E. Use of Proteomics to Demonstrate a Hierarchical Oxidative Stress Response to Diesel Exhaust Particle Chemicals in a Macrophage Cell Line. *J. Biol. Chem.* **2003**, *278*, 50781–50790. [CrossRef] [PubMed]
35. Collard, K.J. Iron homeostasis in the neonate. *Pediatrics* **2009**, *123*, 1208–1216. [CrossRef]
36. Kornberg, T.G.; Stueckle, T.A.; Antonini, J.M.; Rojanasakul, Y.; Castranova, V.; Yang, Y.; Rojanasakul, L.W. Potential toxicity and underlying mechanisms associated with pulmonary exposure to iron oxide nanoparticles: Conflicting literature and unclear risk. *Nanomaterials* **2017**, *7*, 307. [CrossRef]
37. Lum, H.; Roebuck, K.A. Oxidant stress and endothelial cell dysfunction. *Am. J. Physiol. Cell Physiol.* **2001**, *280*, C719–C741. [CrossRef]
38. Prabhakar, P.V.; Reddy, U.A.; Singh, S.P.; Balasubramanyam, A.; Rahman, M.F.; Indu Kumari, S.; Agawane, S.B.; Murty, U.S.N.; Grover, P.; Mahboob, M. Oxidative stress induced by aluminum oxide nanomaterials after acute oral treatment in Wistar rats. *J. Appl. Toxicol.* **2012**, *32*, 436–445. [CrossRef]
39. Reddy, U.A.; Prabhakar, P.V.; Mahboob, M. Biomarkers of oxidative stress for in vivo assessment of toxicological effects of iron oxide nanoparticles. *Saudi J. Biol. Sci.* **2017**, *24*, 1172–1180. [CrossRef]
40. Malvindi, M.A.; De Matteis, V.; Galeone, A.; Brunetti, V.; Anyfantis, G.C.; Athanassiou, A.; Cingolani, R.; Pompa, P.P. Toxicity assessment of silica coated iron oxide nanoparticles and biocompatibility improvement by surface engineering. *PLoS ONE* **2014**, *9*, e8583. [CrossRef]
41. Park, E.J.; Umh, H.N.; Choi, D.H.; Cho, M.H.; Choi, W.; Kim, S.W.; Kim, Y.; Kim, J.H. Magnetite- and maghemite-induced different toxicity in murine alveolar macrophage cells. *Arch. Toxicol.* **2014**, *88*, 1607–1618. [CrossRef]
42. Nel, A.; Xia, T.; Mädler, L.; Li, N. Toxic potential of materials at the nanolevel. *Science* **2006**, *311*, 622–627. [CrossRef]

43. Kobayashi, N.; Naya, M.; Endoh, S.; Maru, J.; Yamamoto, K.; Nakanishi, J. Comparative pulmonary toxicity study of nano-TiO_2 particles of different sizes and agglomerations in rats: Different short- and long-term post-instillation results. *Toxicology* **2009**, *264*, 110–118. [CrossRef] [PubMed]
44. Duffin, R.; Tran, L.; Brown, D.; Stone, V.; Donaldson, K. Proinflammogenic effects of low-toxicity and metal nanoparticles in vivo and in vitro: Highlighting the role of particle surface area and surface reactivity. *Inhal. Toxicol.* **2007**, *19*, 849–856. [CrossRef] [PubMed]
45. Lee, J.H.; Ju, J.E.; Kim, B.I.; Pak, P.J.; Choi, E.K.; Lee, H.S.; Chung, N. Rod-shaped iron oxide nanoparticles are more toxic than sphere-shaped nanoparticles to murine macrophage cells. *Environ. Toxicol. Chem.* **2014**, *33*, 2759–2766. [CrossRef] [PubMed]
46. Chen, Z.; Yin, J.J.; Zhou, Y.T.; Zhang, Y.; Song, L.; Song, M.; Hu, S.; Gu, N. Dual enzyme-like activities of iron oxide nanoparticles and their implication for diminishing cytotoxicity. *ACS Nano* **2012**, *6*, 4001–4012. [CrossRef] [PubMed]
47. Longmire, M.; Choyke, P.L.; Kobayashi, H. Clearance properties of nano-sized particles and molecules as imaging agents: Considerations and caveats. *Nanomedicine* **2008**, *3*, 703–717. [CrossRef] [PubMed]
48. Bhattacharya, K.; Davoren, M.; Boertz, J.; Schins, R.P.F.; Hoffmann, E.; Dopp, E. Titanium dioxide nanoparticles induce oxidative stress and DNA-adduct formation but not DNA-breakage in human lung cells. *Part. Fibre Toxicol.* **2009**, *6*. [CrossRef] [PubMed]
49. Patel, D.; Kell, A.; Simard, B.; Deng, J.; Xiang, B.; Lin, H.Y.; Gruwel, M.; Tian, G. Cu^{2+}-labeled, SPION loaded porous silica nanoparticles for cell labeling and multifunctional imaging probes. *Biomaterials* **2010**, *31*, 2866–2873. [CrossRef] [PubMed]
50. Watson, C.; Ge, J.; Cohen, J.; Pyrgiotakis, G.; Engelward, B.P.; Demokritou, P. High-throughput screening platform for engineered nanoparticle-mediated genotoxicity using cometchip technology. *ACS Nano* **2014**, *8*, 2118–2133. [CrossRef]
51. Freyria, F.S.; Bonelli, B.; Tomatis, M.; Ghiazza, M.; Gazzano, E.; Ghigo, D.; Garrone, E.; Fubini, B. Hematite nanoparticles larger than 90 nm show no sign of toxicity in terms of lactate dehydrogenase release, nitric oxide generation, apoptosis, and comet assay in murine alveolar macrophages and human lung epithelial cells. *Chem. Res. Toxicol.* **2012**, *25*, 850–861. [CrossRef] [PubMed]
52. Soenen, S.J.H.; De Cuyper, M. Assessing cytotoxicity of (iron oxide-based) nanoparticles: An overview of different methods exemplified with cationic magnetoliposomes. *Contrast Media Mol. Imaging* **2009**, *4*, 207–219. [CrossRef] [PubMed]
53. Veranth, J.M.; Kaser, E.G.; Veranth, M.M.; Koch, M.; Yost, G.S. Cytokine responses of human lung cells (BEAS-2B) treated with micron-sized and nanoparticles of metal oxides compared to soil dusts. *Part. Fibre Toxicol.* **2007**, *4*. [CrossRef] [PubMed]
54. Soo Choi, H.; Liu, W.; Misra, P.; Tanaka, E.; Zimmer, J.P.; Itty Ipe, B.; Bawendi, M.G.; Frangioni, J.V. Renal clearance of quantum dots. *Nat. Biotechnol.* **2007**, *25*, 1165–1170. [CrossRef] [PubMed]
55. Barrett, T.; Choyke, P.L.; Kobayashi, H. Imaging of the lymphatic system: New horizons. *Contrast Media Mol. Imaging* **2006**, *1*, 230–245. [CrossRef] [PubMed]
56. Deen, W.M.; Lazzara, M.J.; Myers, B.D. Structural determinants of glomerular permeability. *Am. J. Physiol. Ren. Physiol.* **2001**, *281*, F579–F596. [CrossRef] [PubMed]
57. Ohlson, M.; Sörensson, J.; Haraldsson, B. A gel-membrane model of glomerular charge and size selectivity in series. *Am. J. Physiol. Ren. Physiol.* **2001**, *280*, F396–F405. [CrossRef]
58. Stolnik, S.; Illum, L.; Davis, S.S. Long circulating microparticulate drug carriers. *Adv. Drug Deliv. Rev.* **2012**, *64*, 290–301. [CrossRef]
59. Naqvi, S.; Samim, M.; Abdin, M.Z.; Ahmed, F.J.; Maitra, A.N.; Prashant, C.K.; Dinda, A.K. Concentration-dependent toxicity of iron oxide nanoparticles mediated by increased oxidative stress. *Int. J. Nanomed.* **2010**, *5*, 983–989. [CrossRef]
60. Zhu, M.T.; Feng, W.Y.; Wang, Y.; Wang, B.; Wang, M.; Ouyang, H.; Zhao, Y.L.; Chai, Z.F. Particokinetics and extrapulmonary translocation of intratracheally instilled ferric oxide nanoparticles in rats and the potential health risk assessment. *Toxicol. Sci.* **2009**, *107*, 342–351. [CrossRef]
61. Murray, A.R.; Kisin, E.; Inman, A.; Young, S.-H.; Muhammed, M.; Burks, T.; Uheida, A.; Tkach, A.; Waltz, M.; Castranova, V.; et al. Oxidative Stress and Dermal Toxicity of Iron Oxide Nanoparticles In Vitro. *Cell Biochem. Biophys.* **2013**, *67*, 461–476. [CrossRef]

62. Laskar, A.; Eilertsen, J.; Li, W.; Yuan, X.M. SPION primes THP1 derived M2 macrophages towards M1-like macrophages. *Biochem. Biophys. Res. Commun.* **2013**, *441*, 737–742. [CrossRef] [PubMed]
63. Kodali, V.; Littke, M.H.; Tilton, S.C.; Teeguarden, J.G.; Shi, L.; Frevert, C.W.; Wang, W.; Pounds, J.G.; Thrall, B.D. Dysregulation of macrophage activation profiles by engineered nanoparticles. *ACS Nano* **2013**, *7*, 6997–7010. [CrossRef] [PubMed]
64. Park, E.J.; Oh, S.Y.; Lee, S.J.; Lee, K.; Kim, Y.; Lee, B.S.; Kim, J.S. Chronic pulmonary accumulation of iron oxide nanoparticles induced Th1-type immune response stimulating the function of antigen-presenting cells. *Environ. Res.* **2015**, *143*, 138–147. [CrossRef]
65. Beaver, L.M.; Stemmy, E.J.; Schwartz, A.M.; Damsker, J.M.; Constant, S.L.; Ceryak, S.M.; Patierno, S.R. Lung inflammation, injury, and proliferative response after repetitive particulate hexavalent chromium exposure. *Environ. Health Perspect.* **2009**, *117*, 1896–1902. [CrossRef] [PubMed]
66. Ban, M.; Langonné, I.; Huguet, N.; Guichard, Y.; Goutet, M. Iron oxide particles modulate the ovalbumin-induced Th2 immune response in mice. *Toxicol. Lett.* **2013**, *216*, 31–39. [CrossRef] [PubMed]
67. Gustafsson, Å.; Bergström, U.; Ågren, L.; Österlund, L.; Sandström, T.; Bucht, A. Differential cellular responses in healthy mice and in mice with established airway inflammation when exposed to hematite nanoparticles. *Toxicol. Appl. Pharmacol.* **2015**, *288*, 1–11. [CrossRef]
68. Ma, J.Y.; Mercer, R.R.; Barger, M.; Schwegler-Berry, D.; Scabilloni, J.; Ma, J.K.; Castranova, V. Induction of pulmonary fibrosis by cerium oxide nanoparticles. *Toxicol. Appl. Pharmacol.* **2012**, *262*, 255–264. [CrossRef]
69. Park, E.J.; Kim, H.; Kim, Y.; Yi, J.; Choi, K.; Park, K. Inflammatory responses may be induced by a single intratracheal instillation of iron nanoparticles in mice. *Toxicology* **2010**, *275*, 65–71. [CrossRef]
70. Szalay, B.; Tátrai, E.; Nyíro, G.; Vezér, T.; Dura, G. Potential toxic effects of iron oxide nanoparticles in in vivo and in vitro experiments. *J. Appl. Toxicol.* **2012**, *32*, 446–453. [CrossRef]
71. Sadeghi, L.; Yousefi Babadi, V.; Espanani, H.R. Toxic effects of the Fe_2O_3 nanoparticles on the liver and lung tissue. *Bratisl. Med. J.* **2015**, *116*, 373–378. [CrossRef]
72. Srinivas, A.; Rao, P.J.; Selvam, G.; Goparaju, A.; Murthy, B.P.; Reddy, N.P. Oxidative stress and inflammatory responses of rat following acute inhalation exposure to iron oxide nanoparticles. *Hum. Exp. Toxicol.* **2012**, *31*, 1113–1131. [CrossRef] [PubMed]
73. Totsuka, Y.; Ishino, K.; Kato, T.; Goto, S.; Tada, Y.; Nakae, D.; Watanabe, M.; Wakabayashi, K. Magnetite Nanoparticles Induce Genotoxicity in the Lungs of Mice via Inflammatory Response. *Nanomaterials* **2014**, *4*, 175–188. [CrossRef] [PubMed]
74. Campbeli, J.A. Effects of precipitated silica and of iron oxide on the incidence of primary lung tumours in mice. *Br. Med. J.* **1940**, *2*, 275. [CrossRef] [PubMed]
75. Villacis, R.A.R.; Filho, J.S.; Piña, B.; Azevedo, R.B.; Pic-Taylor, A.; Mazzeu, J.F.; Grisolia, C.K. Integrated assessment of toxic effects of maghemite (Γ-Fe_2O_3) nanoparticles in zebrafish. *Aquat. Toxicol.* **2017**, *191*, 219–225. [CrossRef]
76. De Oliveira, G.M.T.; Kist, L.W.; Pereira, T.C.B.; Bortolotto, J.W.; Paquete, F.L.; De Oliveira, E.M.N.; Leite, C.E.; Bonan, C.D.; De Souza Basso, N.R.; Papaleo, R.M.; et al. Transient modulation of acetylcholinesterase activity caused by exposure to dextran-coated iron oxide nanoparticles in brain of adult zebrafish. *Comp. Biochem. Physiol. Part C Toxicol. Pharmacol.* **2014**, *162*, 77–84. [CrossRef]
77. Boyd, J.T.; Doll, R.; Faulds, J.S.; Leiper, J. Cancer of the lung in iron ore (haematite) miners. *Br. J. Ind. Med.* **1970**, *27*, 97–105. [CrossRef]
78. Andujar, P.; Simon-Deckers, A.; Galateau-Sallé, F.; Fayard, B.; Beaune, G.; Clin, B.; Billon-Galland, M.A.; Durupthy, O.; Pairon, J.C.; Doucet, J.; et al. Role of metal oxide nanoparticles in histopathological changes observed in the lung of welders. *Part. Fibre Toxicol.* **2014**, *11*. [CrossRef]
79. Hu, W.J.; Eaton, J.W.; Tang, L. Molecular basis of biomaterial-mediated foreign body reactions. *Blood* **2001**, *98*, 1231–1238. [CrossRef]
80. Vroman, L.; Adams, A.L.; Fischer, G.C.; Munoz, P.C. Interaction of high molecular weight kininogen, factor XII, and fibrinogen in plasma at interfaces. *Blood* **1980**, *55*, 156–159. [CrossRef]
81. Shiba, E.; Lindon, J.N.; Kushner, L.; Matsueda, G.R.; Hawiger, J.; Kloczewiak, M.; Kudryk, B.; Salzman, E.W. Antibody-detectable changes in fibrinogen adsorption affecting platelet activation on polymer surfaces. *Am. J. Physiol. Cell Physiol.* **1991**. [CrossRef]
82. Simak, J.; De Paoli, S. The effects of nanomaterials on blood coagulation in hemostasis and thrombosis. *Wiley Interdiscip. Rev. Nanomed. Nanobiotechnol.* **2017**, *9*. [CrossRef] [PubMed]

83. Simberg, D.; Zhang, W.M.; Merkulov, S.; McCrae, K.; Park, J.H.; Sailor, M.J.; Ruoslahti, E. Contact activation of kallikrein-kinin system by superparamagnetic iron oxide nanoparticles in vitro and in vivo. *J. Control. Release* **2009**, *140*, 301–305. [CrossRef] [PubMed]
84. Simberg, D.; Park, J.H.; Karmali, P.P.; Zhang, W.M.; Merkulov, S.; McCrae, K.; Bhatia, S.N.; Sailor, M.; Ruoslahti, E. Differential proteomics analysis of the surface heterogeneity of dextran iron oxide nanoparticles and the implications for their in vivo clearance. *Biomaterials* **2009**, *30*, 3926–3933. [CrossRef] [PubMed]
85. Strehl, C.; Maurizi, L.; Gaber, T.; Hoff, P.; Broschard, T.; Poole, A.R.; Hofmann, H.; Buttgereit, F. Modification of the surface of superparamagnetic iron oxide nanoparticles to enable their safe application in humans. *Int. J. Nanomed.* **2016**, *11*, 5883. [CrossRef]
86. Liu, T.; Bai, R.; Zhou, H.; Wang, R.; Liu, J.; Zhao, Y.; Chen, C. The effect of size and surface ligands of iron oxide nanoparticles on blood compatibility. *RSC Adv.* **2020**, *10*. [CrossRef]
87. Escamilla-Rivera, V.; Solorio-Rodríguez, A.; Uribe-Ramírez, M.; Lozano, O.; Lucas, S.; Chagolla-López, A.; Winkler, R.; De Vizcaya-Ruiz, A. Plasma protein adsorption on Fe_3O_4-PEG nanoparticles activates the complement system and induces an inflammatory response. *Int. J. Nanomed.* **2019**. [CrossRef]
88. Laurent, S.; Saei, A.A.; Behzadi, S.; Panahifar, A.; Mahmoudi, M. Superparamagnetic iron oxide nanoparticles for delivery of therapeutic agents: Opportunities and challenges. *Expert Opin. Drug Deliv.* **2014**, *11*, 1449–1470. [CrossRef]
89. Sanjai, C.; Kothan, S.; Gonil, P.; Saesoo, S.; Sajomsang, W. Chitosan-triphosphate nanoparticles for encapsulation of super-paramagnetic iron oxide as an MRI contrast agent. *Carbohydr. Polym.* **2014**, *104*, 231–237. [CrossRef]
90. Naha, P.C.; Al Zaki, A.; Hecht, E.; Chorny, M.; Chhour, P.; Blankemeyer, E.; Yates, D.M.; Witschey, W.R.T.; Litt, H.I.; Tsourkas, A.; et al. Dextran coated bismuth-iron oxide nanohybrid contrast agents for computed tomography and magnetic resonance imaging. *J. Mater. Chem. B* **2014**, *2*, 8239–8248. [CrossRef]
91. Jin, R.; Lin, B.; Li, D.; Ai, H. Superparamagnetic iron oxide nanoparticles for MR imaging and therapy: Design considerations and clinical applications. *Curr. Opin. Pharmacol.* **2014**, *18*, 18–27. [CrossRef]
92. Zaitsev, V.S.; Filimonov, D.S.; Presnyakov, I.A.; Gambino, R.J.; Chu, B. Physical and chemical properties of magnetite and magnetite-polymer nanoparticles and their colloidal dispersions. *J. Colloid Interface Sci.* **1999**, *212*, 49–57. [CrossRef] [PubMed]
93. Hajesmaeelzadeh, F.; Shanehsazzadeh, S.; Grüttner, C.; Daha, F.J.; Oghabian, M.A. Effect of coating thickness of iron oxide nanoparticles on their relaxivity in the MRI. *Iran. J. Basic Med. Sci.* **2016**, *19*, 166–171. [PubMed]
94. Tian, F.; Chen, G.; Yi, P.; Zhang, J.; Li, A.; Zhang, J.; Zheng, L.; Deng, Z.; Shi, Q.; Peng, R.; et al. Fates of Fe_3O_4 and Fe_3O_4 at SiO_2 nanoparticles in human mesenchymal stem cells assessed by synchrotron radiation-based techniques. *Biomaterials* **2014**, *35*, 6412–6421. [CrossRef] [PubMed]
95. Lévy, M.; Lagarde, F.; Maraloiu, V.A.; Blanchin, M.G.; Gendron, F.; Wilhelm, C.; Gazeau, F. Degradability of superparamagnetic nanoparticles in a model of intracellular environment: Follow-up of magnetic, structural and chemical properties. *Nanotechnology* **2010**, *21*. [CrossRef] [PubMed]
96. Cengelli, F.; Maysinger, D.; Tschudi-Monnet, F.; Montet, X.; Corot, C.; Petri-Fink, A.; Hofmann, H.; Juillerat-Jeanneret, L. Interaction of functionalized superparamagnetic iron oxide nanoparticles with brain structures. *J. Pharmacol. Exp. Ther.* **2006**, *318*, 108–116. [CrossRef] [PubMed]
97. Bourrinet, P.; Bengele, H.H.; Bonnemain, B.; Dencausse, A.; Idee, J.M.; Jacobs, P.M.; Lewis, J.M. Preclinical safety and pharmacokinetic profile of ferumoxtran-10, an ultrasmall superparamagnetic iron oxide magnetic resonance contrast agent. *Investig. Radiol.* **2006**, *41*, 313–324. [CrossRef]
98. Bulte, J.W.M.; Hoekstra, Y.; Kamman, R.L.; Magin, R.L.; Webb, A.G.; Briggs, R.W.; Gwan Go, K.; Hulstaert, C.E.; Miltenyi, S.; Hauw The, T.; et al. Specific MR imaging of human lymphocytes by monoclonal antibody-guided dextran-magnetite particles. *Magn. Reson. Med.* **1992**, *25*, 148–157. [CrossRef]
99. Weissleder, R.; Lee, A.S.; Khaw, B.A.; Shen, T.; Brady, T.J. Antimyosin-labeled monocrystalline iron oxide allows detection of myocardial infarct: MR antibody imaging. *Radiology* **1992**, *182*, 381–385. [CrossRef]
100. Yeh, T.-C.; Zhang, W.; Ildstad, S.T.; Ho, C. In Vivo Dynamic MRI Tracking of Rat T-Cells Labeled with Superparamagnetic Iron-Oxide Particles. *Magn. Reson. Med.* **1995**, *33*, 200–208. [CrossRef]
101. Beckmann, N.; Cannet, C.; Fringeli-Tanner, M.; Baumann, D.; Pally, C.; Bruns, C.; Zerwes, H.G.; Andriambeloson, E.; Bigaud, M. Macrophage labeling by SPIO as an early marker of allograft chronic rejection in a rat model of kidney transplantation. *Magn. Reson. Med.* **2003**, *49*, 459–467. [CrossRef]

102. Madru, R.; Kjellman, P.; Olsson, F.; Wingårdh, K.; Ingvar, C.; Ståhlberg, F.; Olsrud, J.; Lätt, J.; Fredriksson, S.; Knutsson, L.; et al. 99mTc-labeled superparamagnetic iron oxide nanoparticles for multimodality SPECT/MRI of sentinel lymph nodes. *J. Nucl. Med.* **2012**, *53*, 459–463. [CrossRef] [PubMed]
103. Chavhan, G.B.; Babyn, P.S.; Thomas, B.; Shroff, M.M.; Mark Haacke, E. Principles, techniques, and applications of T2*-based MR imaging and its special applications. *Radiographics* **2009**, *29*, 1433–1449. [CrossRef] [PubMed]
104. Dunn, S.E.; Brindley, A.; Davis, S.S.; Davies, M.C.; Illum, L. Polystyrene-Poly (Ethylene Glycol) (PS-PEG2000) Particles as Model Systems for Site Specific Drug Delivery. 2. The Effect of PEG Surface Density on the in Vitro Cell Interaction and in VivoBiodistribution. *Pharm. Res. Off. J. Am. Assoc. Pharm. Sci.* **1994**, *11*, 1016–1022. [CrossRef]
105. Briley-Saebo, K.; Bjørnerud, A.; Grant, D.; Ahlstrom, H.; Berg, T.; Kindberg, G.M. Hepatic cellular distribution and degradation of iron oxide nanoparticles following single intravenous injection in rats: Implications for magnetic resonance imaging. *Cell Tissue Res.* **2004**, *316*, 315–323. [CrossRef] [PubMed]
106. Chakravarty, R.; Valdovinos, H.F.; Chen, F.; Lewis, C.M.; Ellison, P.A.; Luo, H.; Meyerand, M.E.; Nickles, R.J.; Cai, W. Intrinsically germanium-69-labeled iron oxide nanoparticles: Synthesis and in-vivo dual-modality PET/MR zimaging. *Adv. Mater.* **2014**, *26*, 5119–5123. [CrossRef]
107. Al Faraj, A.; Shaik, A.P.; Shaik, A.S. Effect of surface coating on the biocompatibility and in vivo MRI detection of iron oxide nanoparticles after intrapulmonary administration. *Nanotoxicology* **2015**, *9*, 825–834. [CrossRef]
108. Hayashi, K.; Nakamura, M.; Sakamoto, W.; Yogo, T.; Miki, H.; Ozaki, S.; Abe, M.; Matsumoto, T.; Ishimura, K. Superparamagnetic nanoparticle clusters for cancer theranostics combining magnetic resonance imaging and hyperthermia treatment. *Theranostics* **2013**, *3*, 366–376. [CrossRef]
109. Alcalá, M.D.; Real, C. Synthesis based on the wet impregnation method and characterization of iron and iron oxide-silica nanocomposites. *Solid State Ion.* **2006**, *177*, 955–960. [CrossRef]
110. Ma, D.; Guan, J.; Normandin, F.; Dénommée, S.; Enright, G.; Veres, T.; Simard, B. Multifunctional nano-architecture for biomedical applications. *Chem. Mater.* **2006**, *18*, 1920–1927. [CrossRef]
111. Tsai, C.P.; Hung, Y.; Chou, Y.H.; Huang, D.M.; Hsiao, J.K.; Chang, C.; Chen, Y.C.; Mou, C.Y. High-contrast paramagnetic fluorescent mesoporous silica nanorods as a multifunctional cell-imaging probe. *Small* **2008**, *4*, 186–191. [CrossRef]
112. Petri-Fink, A.; Steitz, B.; Finka, A.; Salaklang, J.; Hofmann, H. Effect of cell media on polymer coated superparamagnetic iron oxide nanoparticles (SPIONs): Colloidal stability, cytotoxicity, and cellular uptake studies. *Eur. J. Pharm. Biopharm.* **2008**, *68*, 129–137. [CrossRef] [PubMed]
113. Chastellain, M.; Petri, A.; Hofmann, H. Particle size investigations of a multistep synthesis of PVA coated superparamagnetic nanoparticles. *J. Colloid Interface Sci.* **2004**, *278*, 353–360. [CrossRef]
114. Luchini, A.; Vitiello, G. Understanding the nano-bio interfaces: Lipid-coatings for inorganic nanoparticles as promising strategy for biomedical applications. *Front. Chem.* **2019**, *7*, 343. [CrossRef] [PubMed]
115. Fu, R.; Gill, R.L.; Kim, E.Y.; Briley, N.E.; Tyndall, E.R.; Xu, J.; Li, C.; Ramamurthi, K.S.; Flanagan, J.M.; Tian, F. Spherical Nanoparticle Supported Lipid Bilayers for the Structural Study of Membrane Geometry-Sensitive Molecules. *J. Am. Chem. Soc.* **2015**, *137*, 14031–14034. [CrossRef] [PubMed]
116. Choi, J.Y.; Ramasamy, T.; Kim, S.Y.; Kim, J.; Ku, S.K.; Youn, Y.S.; Kim, J.R.; Jeong, J.H.; Choi, H.G.; Yong, C.S.; et al. PEGylated lipid bilayer-supported mesoporous silica nanoparticle composite for synergistic co-delivery of axitinib and celastrol in multi-targeted cancer therapy. *Acta Biomater.* **2016**, *39*, 94–105. [CrossRef] [PubMed]
117. Durfee, P.N.; Lin, Y.S.; Dunphy, D.R.; Muñiz, A.J.; Butler, K.S.; Humphrey, K.R.; Lokke, A.J.; Agola, J.O.; Chou, S.S.; Chen, I.M.; et al. Mesoporous Silica Nanoparticle-Supported Lipid Bilayers (Protocells) for Active Targeting and Delivery to Individual Leukemia Cells. *ACS Nano* **2016**, *10*, 8325–8345. [CrossRef]
118. Liu, J.; Stace-Naughton, A.; Jiang, X.; Brinker, C.J. Porous nanoparticle supported lipid bilayers (protocells) as delivery vehicles. *J. Am. Chem. Soc.* **2009**, *131*, 1354–1355. [CrossRef]
119. Savarala, S.; Ahmed, S.; Ilies, M.A.; Wunder, S.L. Formation and colloidal stability of dmpc supported lipid bilayers on SiO_2 nanobeads. *Langmuir* **2010**, *26*, 12081–12088. [CrossRef]
120. Laurent, S.; Forge, D.; Port, M.; Roch, A.; Robic, C.; Vander Elst, L.; Muller, R.N. Magnetic iron oxide nanoparticles: Synthesis, stabilization, vectorization, physicochemical characterizations and biological applications. *Chem. Rev.* **2008**, *108*, 2064–2110. [CrossRef]
121. Rao, C.N.R.; Ramakrishna Matte, H.S.S.; Voggu, R.; Govindaraj, A. Recent progress in the synthesis of inorganic nanoparticles. *Dalt. Trans.* **2012**, *41*, 5089–5120. [CrossRef]

122. Luchini, A.; Irace, C.; Santamaria, R.; Montesarchio, D.; Heenan, R.K.; Szekely, N.; Flori, A.; Menichetti, L.; Paduano, L. Phosphocholine-decorated superparamagnetic iron oxide nanoparticles: Defining the structure and probing: In vivo applications. *Nanoscale* **2016**, *8*, 10078–10086. [CrossRef] [PubMed]
123. Luchini, A.; Gerelli, Y.; Fragneto, G.; Nylander, T.; Pálsson, G.K.; Appavou, M.S.; Paduano, L. Neutron Reflectometry reveals the interaction between functionalized SPIONs and the surface of lipid bilayers. *Colloids Surf. B Biointerfaces* **2017**, *151*, 76–87. [CrossRef] [PubMed]
124. Pavel, I.A.; Girardon, M.; El Hajj, S.; Parant, S.; Amadei, F.; Kaufmann, S.; Tanaka, M.; Fierro, V.; Celzard, A.; Canilho, N.; et al. Lipid-coated mesoporous silica microparticles for the controlled delivery of β-galactosidase into intestines. *J. Mater. Chem. B* **2018**, *6*, 5633–5639. [CrossRef] [PubMed]
125. Van Schooneveld, M.M.; Vucic, E.; Koole, R.; Zhou, Y.; Stocks, J.; Cormode, D.P.; Tang, C.Y.; Gordon, R.E.; Nicolay, K.; Meijerink, A.; et al. Improved biocompatibility and pharmacokinetics of silica nanoparticles by means of a lipid coating: A multimodality investigation. *Nano Lett.* **2008**, *8*, 2517–2525. [CrossRef]
126. Simeone, L.; Mangiapia, G.; Vitiello, G.; Irace, C.; Colonna, A.; Ortona, O.; Montesarchio, D.; Paduano, L. Cholesterol-based nucleolipid-ruthenium complex stabilized by lipid aggregates for antineoplastic therapy. *Bioconjug. Chem.* **2012**, *23*, 758–770. [CrossRef]
127. Patil-Sen, Y.; Torino, E.; De Sarno, F.; Ponsiglione, A.M.; Chhabria, V.; Ahmed, W.; Mercer, T. Biocompatible superparamagnetic core-shell nanoparticles for potential use in hyperthermia-enabled drug release and as an enhanced contrast agent. *Nanotechnology* **2020**, *31*. [CrossRef]
128. Shukla, S.; Jadaun, A.; Arora, V.; Sinha, R.K.; Biyani, N.; Jain, V.K. In vitro toxicity assessment of chitosan oligosaccharide coated iron oxide nanoparticles. *Toxicol. Rep.* **2015**, *2*, 27–39. [CrossRef]
129. Jain, T.K.; Morales, M.A.; Sahoo, S.K.; Leslie-Pelecky, D.L.; Labhasetwar, V. Iron oxide nanoparticles for sustained delivery of anticancer agents. *Mol. Pharm.* **2005**, *2*, 194–205. [CrossRef]
130. Sitharaman, B.; Tran, L.A.; Pham, Q.P.; Bolskar, R.D.; Muthupillai, R.; Flamm, S.D.; Mikos, A.G.; Wilson, L.J. Gadofullerenes as nanoscale magnetic labels for cellular MRI. *Contrast Media Mol. Imaging* **2007**, *2*, 139–146. [CrossRef]
131. Chen, J.; Saeki, F.; Wiley, B.J.; Cang, H.; Cobb, M.J.; Li, Z.Y.; Au, L.; Zhang, H.; Kimmey, M.B.; Li, X.; et al. Gold nanocages: Bioconjugation and their potential use as optical imaging contrast agents. *Nano Lett.* **2005**, *5*, 473–477. [CrossRef]
132. Cochran, D.B.; Wattamwar, P.P.; Wydra, R.; Hilt, J.Z.; Anderson, K.W.; Eitel, R.E.; Dziubla, T.D. Suppressing iron oxide nanoparticle toxicity by vascular targeted antioxidant polymer nanoparticles. *Biomaterials* **2013**, *34*, 9615–9622. [CrossRef] [PubMed]
133. Somasundaran, P.; Chakraborty, S.; Qiang, Q.; Deo, P.; Wang, J.; Zhang, R. Surfactants, polymers and their nanoparticles for personal care applications. *J. Cosmet. Sci.* **2004**, *55*, 135–136. [CrossRef]
134. Wang, H.; Kumar, R.; Nagesha, D.; Duclos, R.I.; Sridhar, S.; Gatley, S.J. Integrity of 111In-radiolabeled superparamagnetic iron oxide nanoparticles in the mouse. *Nucl. Med. Biol.* **2015**, *42*, 65–70. [CrossRef] [PubMed]
135. Bates, D.; Abraham, S.; Campbell, M.; Zehbe, I.; Curiel, L. Development and characterization of an antibody-labeled super-paramagnetic iron oxide contrast agent targeting prostate cancer cells for magnetic resonance imaging. *PLoS ONE* **2014**, *9*, e97220. [CrossRef] [PubMed]
136. Larson, T.A.; Bankson, J.; Aaron, J.; Sokolov, K. Hybrid plasmonic magnetic nanoparticles as molecular specific agents for MRI/optical imaging and photothermal therapy of cancer cells. *Nanotechnology* **2007**, *18*. [CrossRef]
137. Subbiahdoss, G.; Sharifi, S.; Grijpma, D.W.; Laurent, S.; Van Der Mei, H.C.; Mahmoudi, M.; Busscher, H.J. Magnetic targeting of surface-modified superparamagnetic iron oxide nanoparticles yields antibacterial efficacy against biofilms of gentamicin-resistant staphylococci. *Acta Biomater.* **2012**, *8*, 2047–2055. [CrossRef]
138. Yu, M.K.; Park, J.; Jon, S. Targeting strategies for multifunctional nanoparticles in cancer imaging and therapy. *Theranostics* **2012**, *2*, 3–44. [CrossRef]
139. Moroz, P.; Jones, S.K.; Gray, B.N. Magnetically mediated hyperthermia: Current status and future directions. *Int. J. Hyperth.* **2002**, *18*, 267–284. [CrossRef]
140. Steeves, R.A. Hyperthermia in cancer therapy: Where are we today and where are we going? *Bull. N. Y. Acad. Med. J. Urban Heal.* **1992**, *68*, 341–350.
141. Christophi, C.; Winkworth, A.; Muralihdaran, V.; Evans, P. The treatment of malignancy by hyperthermia. *Surg. Oncol.* **1998**, *7*, 83–90. [CrossRef]

142. Kolosnjaj-Tabi, J.; Di Corato, R.; Lartigue, L.; Marangon, I.; Guardia, P.; Silva, A.K.A.; Luciani, N.; Clément, O.; Flaud, P.; Singh, J.V.; et al. Heat-generating iron oxide nanocubes: Subtle "destructurators" of the tumoral microenvironment. *ACS Nano* **2014**, *8*, 4268–4283. [CrossRef] [PubMed]
143. Johannsen, M.; Gneveckow, U.; Taymoorian, K.; Thiesen, B.; Waldöfner, N.; Scholz, R.; Jung, K.; Jordan, A.; Wust, P.; Loening, S.A. Morbidity and quality of life during thermotherapy using magnetic nanoparticles in locally recurrent prostate cancer: Results of a prospective phase I trial. *Int. J. Hyperth.* **2007**, *23*, 315–323. [CrossRef] [PubMed]
144. Destouches, D.; Page, N.; Hamma-Kourbali, Y.; Machi, V.; Chaloin, O.; Frechault, S.; Birmpas, C.; Katsoris, P.; Beyrath, J.; Albanese, P.; et al. A simple approach to cancer therapy afforded by multivalent pseudopeptides that target cell-surface nucleoproteins. *Cancer Res.* **2011**, *71*, 3296–3305. [CrossRef] [PubMed]
145. Maier-Hauff, K.; Ulrich, F.; Nestler, D.; Niehoff, H.; Wust, P.; Thiesen, B.; Orawa, H.; Budach, V.; Jordan, A. Efficacy and safety of intratumoral thermotherapy using magnetic iron-oxide nanoparticles combined with external beam radiotherapy on patients with recurrent glioblastoma multiforme. *J. Neurooncol.* **2011**, *103*, 317–324. [CrossRef]
146. Matsumine, A.; Takegami, K.; Asanuma, K.; Matsubara, T.; Nakamura, T.; Uchida, A.; Sudo, A. A novel hyperthermia treatment for bone metastases using magnetic materials. *Int. J. Clin. Oncol.* **2011**, *16*, 101–108. [CrossRef]
147. Guardia, P.; Di Corato, R.; Lartigue, L.; Wilhelm, C.; Espinosa, A.; Garcia-Hernandez, M.; Gazeau, F.; Manna, L.; Pellegrino, T. Water-soluble iron oxide nanocubes with high values of specific absorption rate for cancer cell hyperthermia treatment. *ACS Nano* **2012**, *6*, 3080–3091. [CrossRef]
148. Hergt, R.; Dutz, S. Magnetic particle hyperthermia-biophysical limitations of a visionary tumour therapy. *J. Magn. Magn. Mater.* **2007**, *311*, 187–192. [CrossRef]
149. Gawęda, W.; Osial, M.; Żuk, M.; Pękała, M.; Bilewicz, A.; Krysinski, P. Lanthanide-doped SPIONs bioconjugation with trastuzumab for potential multimodal anticancer activity and magnetic hyperthermia. *Nanomaterials* **2020**, *10*, 288. [CrossRef]
150. Piazza, R.D.; Viali, W.R.; Dos Santos, C.C.; Nunes, E.S.; Marques, R.F.C.; Morais, P.C.; Da Silva, S.W.; Coaquira, J.A.H.; Jafelicci, M. PEGlatyon-SPION surface functionalization with folic acid for magnetic hyperthermia applications. *Mater. Res. Express* **2020**, *7*. [CrossRef]
151. Weiss, R.B. Hypersensitivity reactions from taxol. *J. Clin. Oncol.* **1990**, *8*, 1263–1268. [CrossRef]
152. Gelderblom, H.; Verweij, J.; Van Zomeren, D.M.; Buijs, D.; Ouwens, L.; Nooter, K.; Stoter, G.; Sparreboom, A. Influence of cremophor EL on the bioavailability of intraperitoneal paclitaxel. *Clin. Cancer Res.* **2002**, *8*, 1237–1241. [PubMed]
153. Alexiou, C.; Arnold, W.; Klein, R.J.; Parak, F.G.; Hulin, P.; Bergemann, C.; Erhardt, W.; Wagenpfeil, S.; Lubbe, A.S. Locoregional cancer treatment with magnetic drug targeting. *Cancer Res.* **2000**, *60*, 6641–6648. [PubMed]
154. Hu, S.H.; Liao, B.J.; Chiang, C.S.; Chen, P.J.; Chen, I.W.; Chen, S.Y. Core-shell nanocapsules stabilized by single-component polymer and nanoparticles for magneto-chemotherapy/hyperthermia with multiple drugs. *Adv. Mater.* **2012**, *24*, 3627–3632. [CrossRef] [PubMed]
155. Basuki, J.S.; Duong, H.T.T.; Macmillan, A.; Erlich, R.B.; Esser, L.; Akerfeldt, M.C.; Whan, R.M.; Kavallaris, M.; Boyer, C.; Davis, T.P. Using fluorescence lifetime imaging microscopy to monitor theranostic nanoparticle uptake and intracellular doxorubicin release. *ACS Nano* **2013**, *7*, 10175–10189. [CrossRef] [PubMed]
156. Ashley, C.E.; Carnes, E.C.; Phillips, G.K.; Padilla, D.; Durfee, P.N.; Brown, P.A.; Hanna, T.N.; Liu, J.; Phillips, B.; Carter, M.B.; et al. The targeted delivery of multicomponent cargos to cancer cells by nanoporous particle-supported lipid bilayers. *Nat. Mater.* **2011**, *10*, 389–397. [CrossRef] [PubMed]
157. Butler, K.S.; Durfee, P.N.; Theron, C.; Ashley, C.E.; Carnes, E.C.; Brinker, C.J. Protocells: Modular Mesoporous Silica Nanoparticle-Supported Lipid Bilayers for Drug Delivery. *Small* **2016**, *12*, 2173–2185. [CrossRef] [PubMed]
158. Liu, X.; Situ, A.; Kang, Y.; Villabroza, K.R.; Liao, Y.; Chang, C.H.; Donahue, T.; Nel, A.E.; Meng, H. Irinotecan Delivery by Lipid-Coated Mesoporous Silica Nanoparticles Shows Improved Efficacy and Safety over Liposomes for Pancreatic Cancer. *ACS Nano* **2016**, *10*, 2702–2715. [CrossRef]
159. Liang, J.; Zhang, X.; Miao, Y.; Li, J.; Gan, Y. Lipid-coated iron oxide nanoparticles for dual-modal imaging of hepatocellular carcinoma. *Int. J. Nanomed.* **2017**, *12*, 2033–2044. [CrossRef]

160. Traini, G.; Ruiz-de-Angulo, A.; Blanco-Canosa, J.B.; Zamacola Bascarán, K.; Molinaro, A.; Silipo, A.; Escors, D.; Mareque-Rivas, J.C. Cancer Immunotherapy of TLR4 Agonist–Antigen Constructs Enhanced with Pathogen-Mimicking Magnetite Nanoparticles and Checkpoint Blockade of PD-L1. *Small* **2019**, *15*. [CrossRef]
161. Kang, J.H.; Ko, Y.T. Lipid-coated gold nanocomposites for enhanced cancer therapy. *Int. J. Nanomed.* **2015**, *10*, 33–45. [CrossRef]
162. Hamilton, D.J.; Coffman, M.D.; Knight, J.D.; Reed, S.M. Lipid-Coated Gold Nanoparticles and FRET Allow Sensitive Monitoring of Liposome Clustering Mediated by the Synaptotagmin-7 C2A Domain. *Langmuir* **2017**, *33*, 9222–9230. [CrossRef] [PubMed]
163. Allam, A.A.; Sadat, M.E.; Potter, S.J.; Mast, D.B.; Mohamed, D.F.; Habib, F.S.; Pauletti, G.M. Stability and magnetically induced heating behavior of lipid-coated Fe_3O_4 nanoparticles. *Nanoscale Res. Lett.* **2013**, *8*, 1–7. [CrossRef] [PubMed]
164. Thomas, C.E.; Ehrhardt, A.; Kay, M.A. Progress and problems with the use of viral vectors for gene therapy. *Nat. Rev. Genet.* **2003**, *4*, 346–358. [CrossRef] [PubMed]
165. Omuro, A.; DeAngelis, L.M. Glioblastoma and other malignant gliomas: A clinical review. *JAMA J. Am. Med. Assoc.* **2013**, *310*, 1842–1850. [CrossRef] [PubMed]
166. Fang, C.; Wang, K.; Stephen, Z.R.; Mu, Q.; Kievit, F.M.; Chiu, D.T.; Press, O.W.; Zhang, M. Temozolomide nanoparticles for targeted glioblastoma therapy. *ACS Appl. Mater. Interfaces* **2015**, *7*, 6674–6682. [CrossRef]
167. Xing, R.; Liu, G.; Zhu, J.; Hou, Y.; Chen, X. Functional magnetic nanoparticles for non-viral gene delivery and MR imaging. *Pharm. Res.* **2014**, *31*, 1377–1389. [CrossRef]
168. Cheng, R.; Feng, F.; Meng, F.; Deng, C.; Feijen, J.; Zhong, Z. Glutathione-responsive nano-vehicles as a promising platform for targeted intracellular drug and gene delivery. *J. Control. Release* **2011**, *152*, 2–12. [CrossRef]
169. Kievit, F.M.; Stephen, Z.R.; Wang, K.; Dayringer, C.J.; Sham, J.G.; Ellenbogen, R.G.; Silber, J.R.; Zhang, M. Nanoparticle mediated silencing of DNA repair sensitizes pediatric brain tumor cells to γ-irradiation. *Mol. Oncol.* **2015**, *9*, 1071–1080. [CrossRef]
170. Moan, J.; Berg, K. The Photodegradation of Porphyrins in Cells Can Be Used To Estimate the Lifetime of Singlet Oxygen. *Photochem. Photobiol.* **1991**, *53*, 549–553. [CrossRef]
171. Weissleder, R. A clearer vision for in vivo imaging: Progress continues in the development of smaller, more penetrable probes for biological imaging. *Nat. Biotechnol.* **2001**, *19*, 316–317. [CrossRef]
172. Kirui, D.K.; Rey, D.A.; Batt, C.A. Gold hybrid nanoparticles for targeted phototherapy and cancer imaging. *Nanotechnology* **2010**, *21*, 105105. [CrossRef] [PubMed]
173. Laurent, S.; Boutry, S.; Mahieu, I.; Elst, L.; Muller, R. Iron Oxide Based MR Contrast Agents: From Chemistry to Cell Labeling. *Curr. Med. Chem.* **2009**, *16*, 4712–4727. [CrossRef] [PubMed]
174. Na, H.B.; Song, I.C.; Hyeon, T. Inorganic nanoparticles for MRI contrast agents. *Adv. Mater.* **2009**, *21*, 2133–2148. [CrossRef]
175. Rudin, M.; Weissleder, R. Molecular imaging in drug discovery and development. *Nat. Rev. Drug Discov.* **2003**, *2*, 123–131. [CrossRef] [PubMed]
176. Zhou, T.; Wu, B.; Xing, D. Bio-modified Fe_3O_4 core/Au shell nanoparticles for targeting and multimodal imaging of cancer cells. *J. Mater. Chem.* **2012**, *22*, 470–477. [CrossRef]
177. Medarova, Z.; Pham, W.; Kim, Y.; Dai, G.; Moore, A. In vivo imaging of tumor response to therapy using a dual-modality imaging strategy. *Int. J. Cancer* **2006**, *118*, 2796–2802. [CrossRef]
178. Veiseh, O.; Sun, C.; Fang, C.; Bhattarai, N.; Gunn, J.; Kievit, F.; Du, K.; Pullar, B.; Lee, D.; Ellenbogen, R.G.; et al. Specific targeting of brain tumors with an optical/magnetic resonance imaging nanoprobe across the blood-brain barrier. *Cancer Res.* **2009**, *69*, 6200–6207. [CrossRef]
179. Devaraj, N.K.; Keliher, E.J.; Thurber, G.M.; Nahrendorf, M.; Weissleder, R. 18F labeled nanoparticles for in Vivo PET-CT imaging. *Bioconjug. Chem.* **2009**, *20*, 397–401. [CrossRef]
180. Bhatnagar, P.; Alauddin, M.; Bankson, J.A.; Kirui, D.; Seifi, P.; Huls, H.; Lee, D.A.; Babakhani, A.; Ferrari, M.; Li, K.C.; et al. Tumor lysing genetically engineered t cells loaded with multi-modal imaging agents. *Sci. Rep.* **2014**, *4*. [CrossRef]
181. Freund, B.; Tromsdorf, U.I.; Bruns, O.T.; Heine, M.; Giemsa, A.; Bartelt, A.; Salmen, S.C.; Raabe, N.; Heeren, J.; Ittrich, H.; et al. A simple and widely applicable method to 59Fe-radiolabel monodisperse superparamagnetic iron oxide nanoparticles for in vivo quantification studies. *ACS Nano* **2012**, *6*, 7318–7325. [CrossRef]

182. Yip, S.; Christofides, A.; Banerji, S.; Downes, M.R.; Izevbaye, I.; Lo, B.; MacMillan, A.; McCuaig, J.; Stockley, T.; Yousef, G.M.; et al. A Canadian guideline on the use of next-generation sequencing in oncology. *Curr. Oncol.* **2019**, *26*, e241–e254. [CrossRef] [PubMed]